



# Statistical Analysis of the Role of Invariant Manifolds on Robust Trajectories

Amlan Sinha\*<sup>ID</sup> and Ryne Beeson<sup>†ID</sup>  
Princeton University, Princeton, New Jersey 08840

<https://doi.org/10.2514/1.G008818>

As low-thrust space missions grow in prevalence, it is becoming increasingly important to design low-thrust trajectories with robustness against unforeseen thruster outages or *missed thrust events*. Accounting for such anomalies is particularly important in chaotic multibody systems, such as the *cislunar* realm, where pertinent dynamical structures constrain the dynamical flow. Yet it remains unclear how these dynamical structures influence robust trajectory design. This paper provides the first comprehensive statistical comparison between nonrobust and robust trajectories in relation to the invariant manifolds of resonant orbits in a circular restricted three-body problem. For both the nonrobust and robust solution categories, the optimal subset exhibits stronger alignment with the invariant manifolds, whereas the broader feasible set can sometimes deviate significantly. On average, the robust optimal trajectories shadow the invariant manifolds as closely as the nonrobust optimal trajectories and, in some instances, exhibit even stronger alignment than their nonrobust counterparts. By maintaining proximity to these invariant manifolds, the robust low-thrust solutions are able to efficiently leverage the global dynamical flow to achieve optimality even under operational uncertainties.

## Nomenclature

$c$	= nonlinear programming constraints
$\hat{d}_A^S$	= distance along the invariant manifold from the separatrix to its nearest point from any trajectory point
$\bar{d}_A^S(\mathcal{W})$	= distance along the invariant manifold from the separatrix to its nearest point on $\mathcal{W}$ from $x^P \in \{\mathcal{P}(x), \mathcal{P}^{-1}(x)\}$
$\hat{d}_T^S$	= shortest orthogonal distance to any invariant manifold from any trajectory puncture point
$\bar{d}_T^S(\mathcal{W})$	= shortest orthogonal distance to the invariant manifold $\mathcal{W}$ from $x^P \in \{\mathcal{P}(x), \mathcal{P}^{-1}(x)\}$
$\mathcal{F}$ $(\mathcal{F}_t)_{t \geq 0}$	= $\sigma$ -algebra of measurable events filtration representing information over time
$f$	= uncontrolled state vector field
$g$	= controlled state vector field
$\mathcal{I}$	= inequality index set
$J$	= objective function
$\mathcal{L}$	= running cost
$N$	= number of segments
$\mathbb{P}$	= probability measure
$\mathcal{P}(x)$	= forward-integrated trajectory puncture point to $\mathcal{S}$
$\mathcal{P}^{-1}(x)$	= backward-integrated trajectory puncture point to $\mathcal{S}$
$\mathcal{S}$	= Poincaré surface of section
$T_f$	= final coast time
$T_i$	= initial coast time
$T_s$	= shooting time
$t_f$	= final time
$t_0$	= initial time
$u$	= spacecraft control
$W_S^{5:6}$	= stable invariant manifold of the 5:6 resonant orbit

Presented as Paper 23-272 at the AAS/AIAA Astrodynamics Specialist Conference, Big Sky, MT, August 13–17, 2023 and Paper 24-221 at the AAS/AIAA Astrodynamics Specialist Conference, Broomfield, CO, August 11–15, 2024; received 29 September 2024; accepted for publication 22 February 2025; published online 9 June 2025. Copyright © 2025 by Amlan Sinha and Ryne Beeson. Published by the American Institute of Aeronautics and Astronautics, Inc., with permission. All requests for copying and permission to reprint should be submitted to CCC at [www.copyright.com](http://www.copyright.com); employ the eISSN 1533-3884 to initiate your request. See also AIAA Rights and Permissions <https://aiaa.org/publications/publish-with-aiaas/rights-and-permissions/>.

\*Ph.D. Candidate, Department of Mechanical and Aerospace Engineering; [amlans@princeton.edu](mailto:amlans@princeton.edu) (Corresponding Author).

<sup>†</sup>Assistant Professor, Department of Mechanical and Aerospace Engineering.

$W_S^{3:4}$	= stable invariant manifold of the 3:4 resonant orbit
$W_U^{3:4}$	= unstable invariant manifold of the 3:4 resonant orbit
$W_U^{5:6}$	= unstable invariant manifold of the 5:6 resonant orbit
$x^P$	= trajectory puncture point on $\mathcal{S}$
$\Delta\tau$	= duration of the missed thrust event
$\phi$	= terminal cost
$\xi$	= spacecraft state
$\mathcal{E}$	= equality index set
$\tau$	= time where a missed thrust event begins
$\gamma$	= periodic orbit
$\Omega$	= random sample space
$\omega$	= random sample

## Superscripts

$\dagger$	= reference solution
$\omega$	= realization solution

## Subscripts

nr	= nonrobust solution
$r$	= robust solution
$i, j, k$	= indices

## I. Introduction

LOW-THRUST (LT) propulsion systems are becoming increasingly popular in space missions, both large strategic science missions (e.g., Hayabusa, Dawn, Hayabusa2, Bepi-Colombo, Lucy, Psyche) and small technology demonstration missions (e.g., Mars Cube One, NEA Scout, Lunar Flashlight), due to their characteristically high specific impulses, which allow a higher effective payload fraction than their impulsive counterparts. However, these LT missions are susceptible to *safe mode events*, which occur if an anomalous event (e.g., impact with space debris) forces the spacecraft to depart from its nominal operating conditions and enter a protective mode during which all thruster operations are switched off—if such a safe mode event coincides with a scheduled thrust arc, it results in what is known as a missed thrust event (MTE). Due to their characteristically long thrust arcs, MTEs are quite common for LT missions [1]. And, unless specifically accounted for during the preliminary mission design phase, MTEs can severely impact the spacecraft's performance and, in some cases, may even result in complete failure depending on the remaining mission time and the available onboard fuel. This can be especially dire in missions

where success depends on certain maneuvers being performed at critical junctures along the trajectory (e.g., flybys).

While robust trajectory design (i.e., the process of designing LT trajectories robust to MTEs, or more concisely, *robust trajectories* from here on) has garnered interest from both industry and academia in the last decade, there exists a research gap in understanding the global geometric properties of the robust solutions in relation to the dynamical structures in multibody systems. Existing literature in the broader area of robust trajectory design can be predominantly categorized into two schools of thought—"missed thrust design" and "missed thrust analysis." The missed thrust design problem focuses on solving an optimization problem that directly incorporates robustness as a performance metric, whereas the missed thrust analysis problem focuses on evaluating the sensitivity of a nominal trajectory to MTEs.

Practical approaches to robust trajectory design are more similar to the latter. They typically involve redesigning a nominal trajectory under various missed thrust scenarios, perhaps with lower duty cycles or with forced coast arcs in carefully chosen points along the trajectory. Depending on the subsequent change in key performance metrics, e.g., propellant usage and/or time of flight, empirical margin allocations are then made in the nominal mission profile. Such an approach was taken with the Dawn mission to ensure that a minimum shutdown time of 28 days could be endured at all points along the nominal trajectory without significantly compromising mission objectives [2,3]. An almost identical analysis was conducted recently for the Psyche mission [4]. Analogous techniques also appear in various studies within existing literature in this area. For example, Laipert and Longuski investigated the changes in the propellant usage and/or time of flight when a nominal trajectory is reoptimized following a single MTE [5]. Building on this work, Laipert and Imken later utilized the same metrics to evaluate how multiple MTEs affect a nominal trajectory, using a Monte Carlo approach with historical missed thrust data from past missions [6]. However, due to the decoupling between the trajectory optimization and the uncertainty quantification inherent to this approach, this strategy inadvertently risks shifting the sensitivity to a different location along the redesigned trajectory and producing solutions that are glaringly suboptimal with respect to the nominal trajectory.

Significant progress has been made in addressing the missed thrust design problem through both deterministic and stochastic approaches. Olympio approached this problem by formulating it as a two-level stochastic optimal control problem [7], while the expected thrust function, assuming a known distribution for MTEs, has been used by Rubinsztein et al. [8]. More general stochastic frameworks, such as stochastic differential dynamic programming [9] and belief optimal control [10], have also been shown to be effective in robust trajectory design. However, as these stochastic approaches typically model the MTEs as Gaussian disturbances, they do not accurately capture their true stochastic nature. More recent approaches explore data-driven methods in an attempt to learn the mapping between the state of the spacecraft after an MTE has occurred and the optimal control sequence going forward using neural networks [11,12] and reinforcement learning [13,14]. These methods, however, only solve a local problem (i.e., small perturbations from the nominal) and are often limited in their ability to generalize to more complex gravitational environments where the LT trajectories are more sensitive to perturbations.

Other strategies in the literature address the missed thrust design problem by formulating optimization problems with constraints on the missed thrust recovery margin (i.e., the maximum amount of time a spacecraft may be allowed to coast while still being able to reach the terminal manifold once thruster operations are resumed) [15]. State-of-the-art approaches extend this concept by lifting the original optimal control problem to a higher dimensional space to solve for a *reference* trajectory (the path we plan to fly) simultaneously with multiple *realization* trajectories (the path we may switch to should an MTE occur) from a priori chosen points along the reference trajectory [16,17]. Since the reference and the realization trajectories are solved simultaneously as a single large

optimization problem, it can quickly run into computational tractability issues as the number of realizations increases. McCarty et al. [16] therefore choose to restrict the study to a small number of realizations, whereas Venigalla et al. [17] suggest an adaptive algorithm to regulate the number of realizations such that the minimum missed thrust recovery margin across all realizations remains above a threshold. In both studies, however, the authors note that applying the method to multibody gravitational models *may be more challenging* due to the inherently chaotic nature of the underlying dynamics. To the best of our knowledge, the study by McCarty et al. is the only instance where the missed thrust design problem has been studied in the context of multibody gravitational environments. However, because they solve for a single-point solution, it fails to elucidate the true topological properties of the robust solution space in complex dynamical environments.

Another approach to incorporate robustness is to leverage knowledge of the natural dynamical flow within the optimization framework. Alizadeh and Villac adopted this approach by modifying the objective function in the optimal control problem to penalize deviations from the natural dynamical flow [18]. However, this penalty term applies to the deviation integral over the entire mission duration, which may inadvertently allow for trajectories that do not align with the natural dynamical flow at all times. With the exception of Alizadeh and Villac, current methods for designing robust trajectories generally do not approach the problem from a dynamical systems perspective. Even in their work, while the trajectories are encouraged to stay close to the natural dynamical flow, the precise relationship between the flow and the resulting trajectories remains unexplored, leaving a gap in fully understanding this connection.

In a series of recent studies by Cox et al., the evolution of dynamical structures in the circular restricted three-body problem (CR3BP) was examined when augmented with LT propulsion (CR3BP + LT), with applications to designing transit and capture trajectories near secondary bodies [19–21]. The authors utilize control curves to establish initial feasibility bounds on the solution space, which are then refined by incorporating geometric constraints derived from invariant manifolds, providing a more targeted exploration of feasible solutions compared to traditional energy-based methods. Their findings highlight the critical importance of using the manifold geometry in narrowing the solution space and creating a framework for exploring control parameter configurations in LT trajectory design within multibody dynamical systems. A key limitation of the CR3BP + LT model lies in its assumption of a constant thrust profile throughout the analysis. While this assumption is particularly useful for studying ballistic transfers, or low-energy and LT solutions with minimal forcing, it falls short of capturing the full complexity of general LT trajectory design. In optimal control problems, both the thrust direction and magnitude typically vary significantly over time, creating a continuously evolving dynamical landscape, which introduces additional complexity to the analysis. The challenge becomes even more pronounced in the context of robust trajectory design, which typically exhibits a higher dimensional solution space. While the CR3BP + LT model seems to provide valuable insights, the inherent assumptions may limit its applicability for analyzing robust LT solutions.

This study explores the relationship between robust LT solutions and the underlying dynamical structures (DS) in multibody gravitational environments, with the ultimate goal of improving the robust trajectory design process by leveraging a deeper understanding of the geometric and topological properties of the solution space. To accomplish this, we begin by situating the missed thrust design problem within the broader framework of robust control, encompassing a wider range of uncertainties, randomness, and stochasticity. Next, we solve for a collection of nonrobust and robust solutions for a specific low-thrust transfer problem. Finally, leveraging tools from dynamical systems theory, we statistically analyze the differences between these two sets of solutions in relation to the invariant structures within the model. In this study, we specifically focus on a minimum fuel transfer between a 3:4 resonant orbit and a 5:6 resonant orbit in the Jupiter–Europa system, a problem that was originally investigated by Anderson and Lo [22] to understand the

role of invariant manifolds in nonrobust LT trajectory design. Their results imply that the nonrobust optimal LT trajectories naturally align with the relevant invariant structures in the system. To demonstrate this, they compare an optimal LT trajectory with the invariant manifolds of unstable resonant orbits in the Jupiter–Europa system through a qualitative visualization on a Poincaré surface of sections, where the intersections made by the optimal trajectory closely shadow those of the invariant manifolds, highlighting the manifolds' role in LT trajectory design. Notably, their optimization algorithm, despite lacking explicit information about invariant manifolds, produced an optimal trajectory that appeared to leverage these manifolds as natural transitory pathways. While we follow a similar approach as Anderson and Lo, we extend their work in three key aspects. First, to rigorously analyze the relationship between trajectories and DS, we introduce distance metrics on a Poincaré surface of section, which allows for a quantitative comparison of robust and nonrobust solutions, moving beyond previous qualitative assessments. Second, we perform a detailed statistical comparison between robust and nonrobust solutions, examining how their dependence on invariant manifolds evolves under varying parameters, such as the initiation and duration of the MTEs. By considering a family of solutions rather than focusing on a single point solution, we elucidate global geometric and topological properties of the solution space in relation to the underlying DS. Finally, we differentiate between feasible and optimal solutions for both robust and nonrobust cases, providing key insights into how the relationship with the invariant manifolds evolves depending on whether the solutions are merely feasible or achieve optimality, highlighting significant differences in how each class of solutions leverages the DS.

The paper is organized as follows: In Sec. II, we present the general robust optimal control problem, which, under certain assumptions, simplifies into the missed thrust design problem we study in this paper. In Sec. III, we state the circular restricted three-body model with a brief discussion to follow on the relevant DS it exhibits, and in Sec. IV, we describe pertinent tools from dynamical systems theory along with the metrics we use to characterize the trajectory solutions with respect to the invariant manifolds. In Sec. V, we first present a qualitative comparison between an example robust solution and an example nonrobust solution and then present a statistical comparison between solution families in each category to uncover differences in their global properties. Finally, we highlight the importance of this work and summarize key insights from this study in Sec. VI.

## II. Robust Optimal Control Problem Formulation

We begin this section by formulating an optimal control problem that accounts for uncertainty in terminal boundary conditions and flight path constraints, randomness in system parameters, and stochastic effects. We start from generality so that the reader has a wider context of the missed thrust design problem considered in this paper and so that future efforts have guidance on where to start additional extensions of the work considered in this paper with respect to additional sources of uncertainty, randomness, and stochasticity. After stating the general problem definition in Sec. II.A, we narrow our focus to the infinite-dimensional missed thrust design problem in Sec. II.B, and then, a finite-dimensional restriction of the missed thrust design formulation is made in Sec. II.C, which allows us to perform the numerical analysis of this paper.

### A. General Robust Formulation

Let  $(\Omega, \mathcal{F}, (\mathcal{F}_t)_{t \geq 0}, \mathbb{P})$  be a filtered probability space. For a given random sample  $\omega \in \Omega$ , consider an optimal control problem where we aim to determine an extremal control solution  $\mathbf{u}^* \in \mathcal{U}$ , with  $\mathcal{U}$  an admissible control set, to minimize the Bolza-type cost functional,

$$\min_{\mathbf{u} \in \mathcal{U}} \left\{ J(\mathbf{u}; \omega) \equiv \phi(\xi_1(\omega)) + \int_0^1 \mathcal{L}(s, \xi_s(\omega), \mathbf{u}_s) ds \right\} \quad (1)$$

such that Eqs. (2–4) are satisfied. We consider the finite-time problem, and without loss of generality, we normalize the time interval to be  $[0, 1]$ . In Eq. (1),  $\xi$  is the solution to a stochastic differential equation driven by the control  $\mathbf{u} \in \mathcal{U}$ ,

$$\begin{aligned} \xi_t(\omega; \mathbf{u}) &= \xi_0(\omega) + \int_0^t f(s, \xi_s(\omega; \mathbf{u}), \omega) ds \\ &\quad + \int_0^t g(s, \xi_s(\omega; \mathbf{u}), \mathbf{u}_s, \omega) d\nu(s, \mathbf{u}_s, \omega), \\ \forall t \in [0, 1], \quad \forall \omega \in \Omega \end{aligned} \quad (2)$$

taking values in a smooth manifold  $\Xi$ , satisfying the probabilistic initial and terminal boundary conditions,

$$\begin{aligned} \mathbb{P}(\xi_0(\omega) \in \Xi_0) &\geq 1 - \epsilon_{\Xi_0}, \quad \text{and} \quad \mathbb{P}(\xi_1(\omega) \in \Xi_1) \geq 1 - \epsilon_{\Xi_1}, \\ \forall \omega \in \Omega \end{aligned} \quad (3)$$

and probabilistic path constraints,

$$\mathbb{P}(\varphi_i(\xi_t(\omega)) \leq 0) \geq 1 - \epsilon_{\varphi}, \quad \forall t \in [0, 1], \quad \forall \omega \in \Omega, \quad \forall \varphi_i \in G \quad (4)$$

The numbers  $\epsilon_{\Xi_0}$ ,  $\epsilon_{\Xi_1}$ , and  $\epsilon_{\varphi}$  take values in the unit interval, and  $G$  is collection of real-valued functions. Readers seeking a more comprehensive understanding of the general robust optimal control problem are directed to several foundational works on stochastic control [23–25].

The optimal control problem above contains several sources of uncertainty, randomness, and stochasticity. For example, the initial condition  $\xi_0(\omega)$  describes aleatoric uncertainty in the spacecraft state due to navigational errors. The drift coefficient  $f(\cdot, \omega)$  represents dynamics that are independent of the control but may also have epistemic uncertainty (e.g., uncertainty in system parameters such as location, mass, or spherical harmonics of a central gravitational body). The dispersion coefficient  $g(\cdot, \omega)$  allows for uncertainty that is dependent on the control input, and  $\nu(\cdot, \omega)$  is a stochastic forcing term that may be dependent on the control process. In the simplest case,  $\nu$  could be a Lebesgue–Stieljes measure or a Brownian motion in an Itô integral definition. If it is simply a Lebesgue measure, then our dynamics are for a random differential equation (e.g., uncertainty in propulsion parameters). Equation (1) therefore includes both endogenous and exogenous uncertainty and naturally accommodates aleatoric and epistemic uncertainty in the space flight problem. The text by Øksendal [26] provides a good introduction to stochastic differential equations (SDEs). The reader can find greater detail on SDEs in Arnold [27] or LeGall [28].

While the optimal control problem in Eq. (1) only measures the cost for a single random sample  $\omega \in \Omega$ , it is natural to consider an objective function that is dependent on the complete set  $\Omega$ , and this can be defined in a general manner by considering the space of linear functionals  $\mathcal{J}$  acting on  $J$ . By the Riesz–Markov–Kakutani theorem [29], we can identify any element in  $\mathcal{J}$  with the action of integrating  $J$  against a measure. Because we are interested in the case where  $\Omega$  is a probability sample space, it is natural for us to restrict  $\mathcal{J}$  to the case where we identify it with probability measures. Therefore, for the general robust problem, we ultimately consider an objective function of the form

$$\psi \circ J(\mathbf{u}; \omega) \equiv \mathbb{E}_{\mathbb{Q}_\psi} \left[ \phi(\xi_1(\omega)) + \int_0^1 \mathcal{L}(s, \xi_s(\omega), \mathbf{u}_s) ds \right] \quad (5)$$

for some  $\psi \in \mathcal{J}$  with identifying probability measure  $\mathbb{Q}_\psi$ . The deterministic case is recovered whenever the probability measure is a Dirac distribution with support on a single sample element,  $\mathbb{Q}_\psi = \delta_\omega$ .

Therefore, the general robust optimal control problem can be stated as follows. Given a cost functional  $\psi \in \mathcal{J}$  over the sample

space  $\Omega$ , we seek a minimizing extremal control solution  $\mathbf{u}^* \in \mathcal{U}$  to the following problem:

$$\min_{\mathbf{u} \in \mathcal{U}} \left\{ \psi \circ J(\mathbf{u}; \omega) \equiv \mathbb{E}_{\mathbb{Q}_\psi} \left[ \phi(\xi_1(\omega)) + \int_0^1 \mathcal{L}(s, \xi_s(\omega), \mathbf{u}_s) ds \right] \right\} \quad (6)$$

such that Eqs. (2–4) are satisfied.

### B. Robust (MTE) Formulation

To derive the (infinite-dimensional) missed thrust design problem from the general robust formulation, we now make several simplifying assumptions. We assume that there is no stochastic forcing in Eq. (2), and hence replace  $d\nu(s, \mathbf{u}_s, \omega)$  with  $ds$ . We also assume that  $f$  contains no randomness and that randomness in  $g$  occurs in a very specific way. In particular, we introduce random times that determine whether the dispersion coefficient (or forcing function)  $g$ , and consequently the control input  $\mathbf{u}$ , affects the state dynamics  $\xi$ . To do this, we let the random sample space be identified with the unit circle (i.e.,  $\Omega \simeq S^1 \simeq [0, 1]$ ), and introduce a collection of positive strictly increasing random times  $\tau \equiv \{\tau_i(\omega) \in \mathbb{R}_+ \mid \tau_i < \tau_{i+1}, \forall i \in \mathbb{Z}_+, \omega \in \Omega\}$ . Given a control function  $\mathbf{u}$ , the dynamics of an MTE trajectory is now explicitly given by

$$\begin{aligned} \xi_t(\omega; \mathbf{u}) = & \xi_0(\omega) + \int_0^t f(s, \xi_s(\omega; \mathbf{u})) ds \\ & + \int_0^{\tau_1(\omega) \wedge t} g(s, \xi_s(\omega; \mathbf{u}), \mathbf{u}_s) ds \\ & + \sum_{i \in \mathbb{Z}_+} \int_{\tau_{2i}(\omega)}^{\tau_{2i+1}(\omega) \wedge t} g(s, \xi_s(\omega; \mathbf{u}), \mathbf{u}_s) ds, \end{aligned} \quad \forall t \in [0, 1], \quad \forall \omega \in \Omega \quad (7)$$

The uncertainty due to the random times  $\tau$  specifies the initiation and duration of the MTE intervals. For a given sample  $\omega \in \Omega$ , an MTE will be initiated if  $\tau_1(\omega) < 1$ , with additional MTEs for any  $\tau_{2i+1}(\omega) < 1$  with  $i \in \mathbb{Z}_+$ . The duration of an MTE is  $\tau_{2(i+1)} - \tau_{2i+1}$  for any  $i \in \mathbb{Z}_+(0)$ . The symbol  $\wedge$  in Eq. (7) is the minimum operator (i.e.,  $a \wedge b = \min(a, b)$ ). For a given realization  $\omega$ , if  $\tau_1(\omega) > 1$ , then no MTE will occur, since we are considering the finite-time problem with  $t \in [0, 1]$ .

We now explicitly define our choice of admissible control sets by defining the set  $\mathcal{U} \equiv PC([0, 1]; \mathbb{R}^n)$  for  $n \in \mathbb{Z}_+$  to be the piecewise continuous functions on  $[0, 1]$ . Our admissible control set will be given by  $\mathcal{U}^\Omega \equiv \mathcal{U}^{S^1}$ , which describes the functions from  $S^1$  into  $\mathcal{U}$  (equivalently  $\prod_{S^1} \mathcal{U}$ ). In what follows, we make the choice that  $\tau_1(0) = \tau_1(1) > 1$ , and hence the sample  $\omega \in \{0, 1\}$  will correspond to a (deterministic) non-MTE trajectory for Eq. (7). We denote this special case, when  $\omega \in \{0, 1\}$ , with the  $\dagger$  symbol as  $\mathbf{u}^\dagger$  and refer to the state solution  $\xi^\dagger$  as the *reference* solution. For all

other cases, when  $\omega \in (0, 1)$ , we denote the control solution as  $\mathbf{u}^\omega$  and refer to the associated state solution  $\xi^\omega$  as a *realization*.

The optimal control problem for the (infinite-dimensional) missed thrust design problem can now be stated as follows. We seek to find an extremal control solution  $\mathbf{u}^* \in \mathcal{U}^\Omega$  to the following problem:

$$\min_{\mathbf{u} \in \mathcal{U}^\Omega} \left\{ J(\mathbf{u}^\dagger) \equiv \phi(\xi_1^\dagger) + \int_0^1 \mathcal{L}(s, \xi_s^\dagger, \mathbf{u}_s^\dagger) ds \right\} \quad (8)$$

such that Eqs. (9), (3), and (4) are satisfied, where the reference and realization dynamics are given by

$$\begin{aligned} \xi_t^\omega = & \xi_0^\omega + \int_0^t f(s, \xi_s^\omega) ds + \int_0^{\tau_1(\omega) \wedge t} g(s, \xi_s^\omega, \mathbf{u}_s^\omega) ds \\ & + \sum_{i \in \mathbb{Z}_+} \int_{\tau_{2i}(\omega)}^{\tau_{2i+1}(\omega) \wedge t} g(s, \xi_s^\omega, \mathbf{u}_s^\omega) ds, \quad \forall t \in [0, 1], \quad \forall \omega \in \Omega \end{aligned} \quad (9)$$

### C. Restricted Robust (MTE) Formulation

The main challenge in solving the robust MTE problem is the definition and approximation of the probability distribution for the random times  $\tau$ , which is necessary for satisfying the dynamical constraints of Eq. (9) that couples the reference and realization solutions. Based on analysis of past LT missions, Imken et al. [1] have suggested that the Weibull distribution is a good fit for the initiation and duration times of an MTE. The Weibull distribution is a continuous distribution and therefore achieving numerical tractability would require some sample approximation. In this paper, we assume a simpler distribution than the Weibull. Our assumptions are more in line with those of McCarty and Grebow [16], and Venigalla et al. [17]. See Fig. 1 for a schematic of the restricted missed thrust problem. We now describe these assumptions, by first stating them in words and then giving the mathematical definitions as subitems:

A1. Only one MTE will occur for any realization.

1) For each  $\omega \in \Omega$ , assume that  $\tau_3(\omega) > 1$ .

A2. Only a finite number of MTE initiations are allowed, with each corresponding to the start of a thrust segment (a shooting transcription is used and will be further explained in Sec. II.D).

1) Assume that  $(0, 1) \subset S^1 = \Omega$  is partitioned into a collection of  $N$  intervals  $(E_i)_{i=1}^N$ .

2) Assume that for every interval  $E_i$ , we have for any  $\omega_0, \omega_1 \in E_i$ , the relation  $\tau_1(\omega_0) = \tau_1(\omega_1)$ .

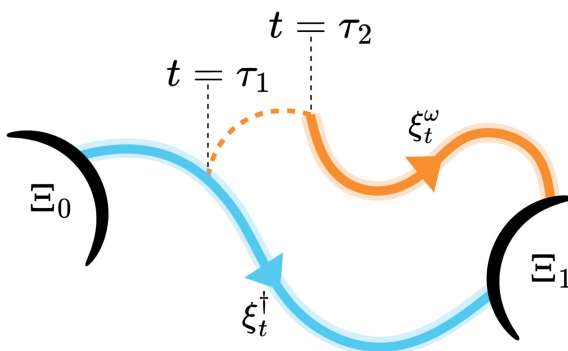
A3. Only a finite number of MTE durations are allowed.

1) Assume that each interval  $E_i$  is further partitioned into a collection of  $M$  subintervals  $(E_{i,j})_{j=1}^M$ .

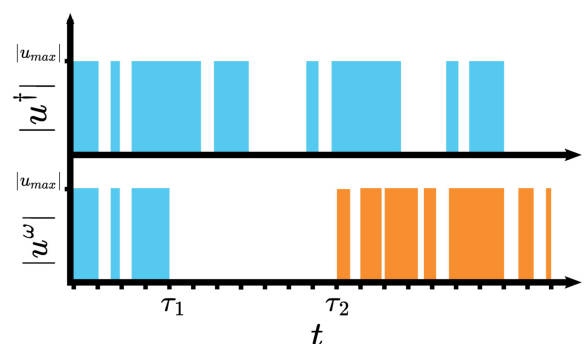
2) Assume that for every subinterval  $E_{i,j}$ , we have for any  $\omega_0, \omega_1 \in E_{i,j}$ , the relation  $\tau_2(\omega_0) = \tau_2(\omega_1)$ .

A4. Enforce deterministic boundary conditions.

1) Assume that  $e_{\Xi_0} = e_{\Xi_1} = 0$ .



a) Schematic of the restricted robust problem showing reference and realization trajectories



b) Schematic of throttle profiles with thruster outage during interval  $t \in [\tau_1, \tau_2]$

Fig. 1 Schematic of restricted robust problem with example reference and realization trajectories, and corresponding throttle profiles.

A5. Assume that no flight path constraint exists (beyond the dynamical constraint).

1) Assume that  $G = \emptyset$  (i.e., the empty set).

A6. Lastly, we will solve NM versions of our robust MTE optimal control problem, with each case corresponding to a different probability distribution  $\mathbb{P}$  on  $\Omega$ .

1) For each  $i \in \{1, \dots, N\}, j \in \{1, \dots, M\}$ , define a robust MTE optimal control problem where  $\mathbb{P}(E_{i,j} \cup \{0, 1\}) = 1$ .

Assumption A1 specifies the number of MTEs we consider in the subsequent analysis. While seemingly restrictive, it is well-supported by statistical evidence from historical missed thrust data [1]. For the range of total thrust arc durations observed in the nonrobust solutions, this single-MTE approach successfully captures approximately 90% of observed scenarios. We sample MTE durations from a distribution fit to representative mission data, encompassing both brief disruptions (0.5 TU, or  $\sim 6.5$  h) and extended outages (30 TU, or  $\sim 17$  days). With longer-duration events accounting for approximately 99% of scenarios, this framework effectively captures both nominal and extreme failure cases (see Fig. 2 for the distribution).

Assumption A6 addresses the spatial and temporal characteristics of MTEs—specifically, where they occur and how long they last. Even within a single-MTE approach, we must consider that the outage could occur at any point in the trajectory. In fact, for a truly comprehensive analysis, we would ideally examine the impact at every point along the reference trajectory where there is a nonzero probability of an MTE, weighting each realization according to the measure of the distribution over the interval it represents. This could potentially result in an infinite number of realizations, i.e., an infinite number of couplings between the reference trajectory and its corresponding realization solutions. The computational complexity of our framework increases significantly with each additional coupling between the reference solution and its realizations. Even with a single MTE with a single coupling (i.e., a single location), generating sufficient solutions for meaningful statistical analysis demands substantial computational resources, given the inherent complexity of optimization in chaotic multibody dynamical systems. While incorporating multiple MTEs would more accurately reflect certain mission profiles, it would significantly increase computational complexity through an expanded sampling space and larger search domain. Our current analysis provides a tractable approach for validating the proposed methods and identifying key trends, providing valuable insights into how invariant manifolds influence robust LT trajectory design, while maintaining both computational feasibility and statistical rigor.

However, we would like to emphasize that the framework we present is readily scalable to accommodate multiple MTEs. Future work will relax the single-event constraint to address multi-event sequences, extending this framework's applicability to a broader range of mission design scenarios, building upon the insights gained from this foundational study.

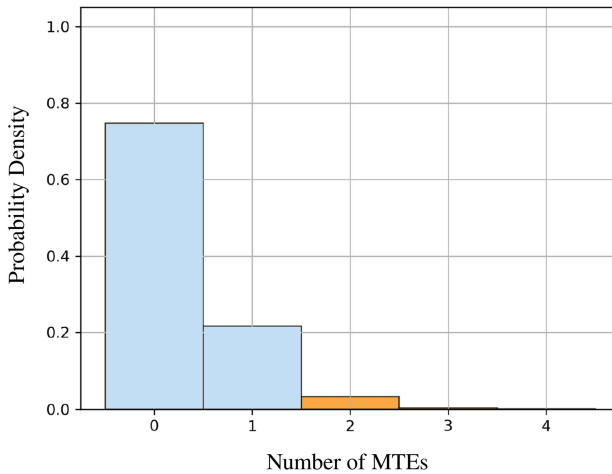


Fig. 2 Distribution of number of MTEs and their durations based on empirical data of past missions (see Imken et al. [1]).

For completeness, we now state the optimal control problem for the restricted missed thrust design problem under the additional assumptions just given,

$$\min_{\mathbf{u} \in \mathcal{U}^\Omega} \left\{ J(\mathbf{u}^\dagger) \equiv \phi(\xi_1^\dagger) + \int_0^1 \mathcal{L}(s, \xi_s^\omega, \mathbf{u}_s^\dagger) ds \right\} \quad (10)$$

such that Eqs. (11) and (12) are satisfied, where the reference and realization dynamics are given by

$$\begin{aligned} \text{s.t. } \xi_t^\omega &= \xi_0^\dagger + \int_0^t f(s, \xi_s^\omega) ds + \int_{\tau_1(\omega)}^{\tau_1(\omega) \wedge t} g(s, \xi_s^\omega, \mathbf{u}_s^\dagger) ds \\ &+ \int_{\tau_2(\omega)}^t g(s, \xi_s^\omega, \mathbf{u}_s^\omega) ds, \quad \forall t \in [0, 1], \quad \forall \omega \in \Omega \end{aligned} \quad (11)$$

satisfying the boundary conditions

$$\xi_0^\omega \in \Xi_0, \quad \xi_1^\omega \in \Xi_1, \quad \forall \omega \in \Omega \quad (12)$$

#### D. Transcription to a Nonlinear Program

In this study, we solve the optimal control problem of Eq. (10) using the Dynamically Leveraged Automated (N) Multibody Trajectory Optimization (DyLAN) software developed by Beeson et al. [30]. DyLAN brings together dynamical systems tools with local and global optimization methods to search for solutions to optimal control problems in multibody environments. A direct approach with a forward-backward shooting transcription is used to convert the optimal control problem into a nonlinear program (NLP). The gradient-based numerical optimizer SNOPT [31] is employed to solve the resulting NLP, with initial guesses generated by the monotonic basin hopping global search algorithm [32–36]. Following the last assumption of Sec. II.C, we fix a version of our robust MTE problem with a probability distribution having  $\mathbb{P}(E_{i,j} \cup \{0, 1\}) = 1$  for some  $i \in \{1, \dots, N\}$  and  $j \in \{1, \dots, M\}$  and then define the NLP as follows:

$$\begin{aligned} \min_{\mathbf{x}^\dagger \in \mathbb{R}^{\bar{N}^\dagger}, \mathbf{x}^\omega \in \mathbb{R}^{\bar{N}^\omega}} \quad & J(\mathbf{x}^\dagger) = -m_f^\dagger, \\ \text{subject to} \quad & c_k^\dagger(\mathbf{x}^\dagger) = 0, \quad c_k^\omega(\mathbf{x}^\omega) = 0, \quad \forall k \in \mathcal{E}, \\ & c_k^\dagger(\mathbf{x}^\dagger) \leq 0, \quad c_k^\omega(\mathbf{x}^\omega) \leq 0, \quad \forall k \in \mathcal{I} \end{aligned} \quad (13)$$

where the index set  $\mathcal{E}$  identifies the equality constraints, which consist of midpoint defect errors for the position, velocity, and mass continuity of the reference and realization. The index set  $\mathcal{I}$  identifies the inequality constraints, which consist of bounds on the control variables for the reference  $\mathbf{x}^\dagger$  and realization  $\mathbf{x}^\omega$ . The reference control decision variable has  $\bar{N}^\dagger = 3N^\dagger + 4$  components given by

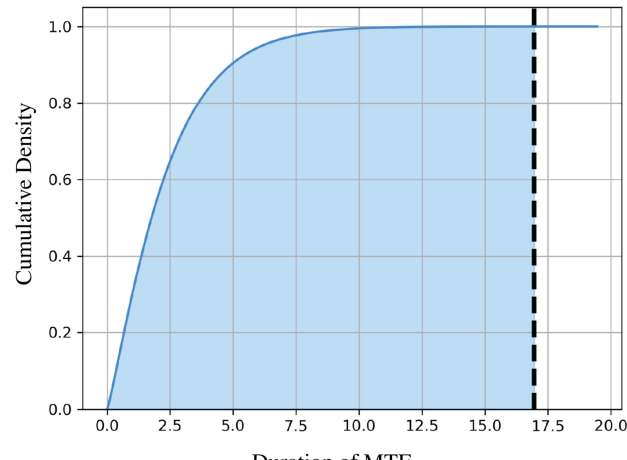


**Table 1 Number of decision variables  
(number of realizations = 1)**

Parameter	Nonrobust	Robust
Number of segments	$N^\dagger$	$N^\dagger + N^\omega$
Control vector components		
Time of flight	3	6
Thrust vector	$3N^\dagger$	$3(N^\dagger + N^\omega)$
Final mass	1	2
Number of constraints	7	14

$$\mathbf{x}^\dagger = \left( T_s^\dagger, T_i^\dagger, T_f^\dagger, u_1^\dagger, u_2^\dagger, \dots, u_{N^\dagger}^\dagger, m_f^\dagger \right) \quad (14)$$

where  $T_s^\dagger$  is the shooting time,  $T_i^\dagger$  the initial coast time, and  $T_f^\dagger$  the final coast time, and, therefore, the total time of flight is  $T_i^\dagger + T_s^\dagger + T_f^\dagger$ . Note that  $u_k^\dagger \in \mathbb{R}^3$  is a constant thrust vector for the  $k$ th thrust segment that represents the throttle, in-plane, and out-of-plane thrust angle. Lastly,  $m_f^\dagger$  is the final delivered wet mass. Therefore, the total number of constraints for the reference solution is equal to  $\bar{N}^\dagger + 7$ , which includes the  $\bar{N}^\dagger$  inequality constraints, and seven equality constraints. The thrust segments each have equal time of  $T_s^\dagger/N^\dagger$ .

The transcription for the realization is similar, but  $\mathbf{x}^\omega$  will contain fewer control variables. The exact number is dependent on when the MTE for  $\mathbf{x}^\omega$  occurs. In particular, the total number of decision variables will be  $\bar{N}^\omega = 3N^\omega + 4 = 3(N^\dagger - i) + 4$ , where the MTE occurs at the start of the  $i$ th thrust segment for the reference solution. This *adaptive segmentation* approach, which is explained in greater detail in Sinha and Beeson [37], promotes congruence in control authority between the reference and realization solutions and therefore enables a more measured understanding of the role of MTEs on the reference control solution. A breakdown of the number of decision variables for both the nonrobust and robust cases is summarized in Table 1. Similar to the reference solution, the number of equality constraints remains unchanged for the realization solution, while the number of inequality constraints becomes  $\bar{N}^\omega$ .

The derivatives of the matchpoint defect errors with respect to the control variables are computed analytically. Analytic derivatives have been extensively studied by Ellison et al. in the context of nonrobust LT trajectory design [38]. To compute the analytic derivatives for the nonrobust solution, we adopt a similar methodology to their approach. In the robust trajectory design problem, however, it becomes necessary to augment the dynamical information by incorporating the flow of derivatives from the reference solution to the realization solutions. For further details on the analytic derivatives, we refer the reader to Sinha and Beeson [37].

### III. Dynamical Model

#### A. Circular Restricted Three-Body Problem

In this study, we consider the motion of a spacecraft in the circular restricted three-body problem (CR3BP) [39–41]. The CR3BP describes the motion of the spacecraft, whose mass is assumed to be negligible, under the influence of two celestial bodies, such as the Earth and the Moon, which rotate about their common center of mass in circular orbits. To elucidate relevant structures in the problem, it becomes convenient to write the spacecraft's equations of motion in a synodic reference frame that rotates at the same rate as the two primaries. The state of the spacecraft in phase space then can be described by a set of scalars  $(q_1, q_2, q_3, \dot{q}_1, \dot{q}_2, \dot{q}_3)$  describing the position and the velocity in the rotating frame. The analysis can be further simplified by nondimensionalizing the equations using a suitable choice of units that reduces the number of parameters in the problem to one, namely, the mass parameter  $\mu = m_2/(m_1 + m_2)$ , where  $m_1$  is the mass of the primary and  $m_2 \leq m_1$  is the mass of the secondary. With this choice of units, the gravitational constant and the mean motion both become unity and lead to the following equations of motion:

$$\begin{aligned} \ddot{q}_1 - 2\dot{q}_2 &= -\frac{\partial \bar{U}}{\partial q_1} + \langle u, \hat{q}_1 \rangle, \\ \ddot{q}_2 + 2\dot{q}_1 &= -\frac{\partial \bar{U}}{\partial q_2} + \langle u, \hat{q}_2 \rangle, \\ \ddot{q}_3 &= -\frac{\partial \bar{U}}{\partial q_3} + \langle u, \hat{q}_3 \rangle \end{aligned} \quad (15)$$

where  $\hat{q}_i$  is the  $i$ th canonical ordinate and  $u$  is the control perturbation;

$$\bar{U}(q_1, q_2, q_3) \equiv -\frac{1}{2} \left( q_1^2 + q_2^2 \right) - \frac{1-\mu}{r_1} - \frac{\mu}{r_2} - \frac{1}{2}(1-\mu)\mu$$

is the *effective* gravitational potential; and

$$\begin{aligned} r_1(q_1, q_2, q_3) &\equiv \sqrt{(q_1 + \mu)^2 + q_2^2 + q_3^2}, \\ r_2(q_1, q_2, q_3) &\equiv \sqrt{(q_1 - (1-\mu))^2 + q_2^2 + q_3^2} \end{aligned}$$

are the distances between the spacecraft to the primary and the secondary, respectively, in the rotating frame coordinate system.

For an LT trajectory, it is also necessary to account for the change in the spacecraft mass, which can be done by simply augmenting the mass to the state of the spacecraft, where the change in the mass  $m$  is governed by the differential equation:

$$\dot{m} = -\frac{|u|}{I_{sp}g} \quad (16)$$

where  $|u|$  is the 2-norm and hence the thrust magnitude,  $g = 9.806 \text{ m/s}^2$  is the gravitational acceleration on Earth, and  $I_{sp}$  is the constant specific impulse of the propulsion system. We neglect any other perturbations on the spacecraft (e.g., solar radiation pressure) such that the only other term perturbing the natural dynamics is the effect of the control input.

In the absence of control perturbations, there exists an integral of motion in the synodic reference frame,

$$C(q_1, q_2, q_3, \dot{q}_1, \dot{q}_2, \dot{q}_3) \equiv -(\dot{q}_1^2 + \dot{q}_2^2 + \dot{q}_3^2) - 2\bar{U}$$

known as the Jacobi integral (or Jacobi constant). The Jacobi integral, which can be thought of as a measure of the *energy* of the spacecraft, remains constant between maneuvers (i.e., the Jacobi integral remains constant during the coast arcs in a spacecraft trajectory).

#### B. Invariant Manifolds of Unstable Periodic Orbits

Despite being relatively simple, this model exhibits rich dynamical properties, yielding a multitude of DS that can be leveraged during LT trajectory design. There exist five equilibrium points in this model known as the libration points. Three of these points,  $\mathcal{L}_1$ ,  $\mathcal{L}_2$ , and  $\mathcal{L}_3$ , are referred to as the collinear equilibrium points as they lie on the line joining the primary and the secondary, and the remaining two points  $\mathcal{L}_4$ ,  $\mathcal{L}_5$ , which form equilateral triangles with the primary and the secondary as other vertices, are referred to as the noncollinear equilibrium points. It was first shown by Poincaré [42] and later by Hénon [43–47] that, in addition to these equilibrium points, there also exists an infinite number of periodic solutions in the three-body model. Since then, various analytical and numerical tools have been developed to compute these periodic orbits in the neighborhood of the Lagrange points for various systems. Each type of periodic orbit has its own distinct features, making them well-suited for specific applications.

The unstable periodic orbits within this dynamical model possess normally hyperbolic *invariant manifolds* [40,48,49]. When we refer to a structure as *invariant*, we imply that it is time-invariant, meaning that these structures remain unchanged throughout the evolution of the dynamical time. Invariant manifolds transport material

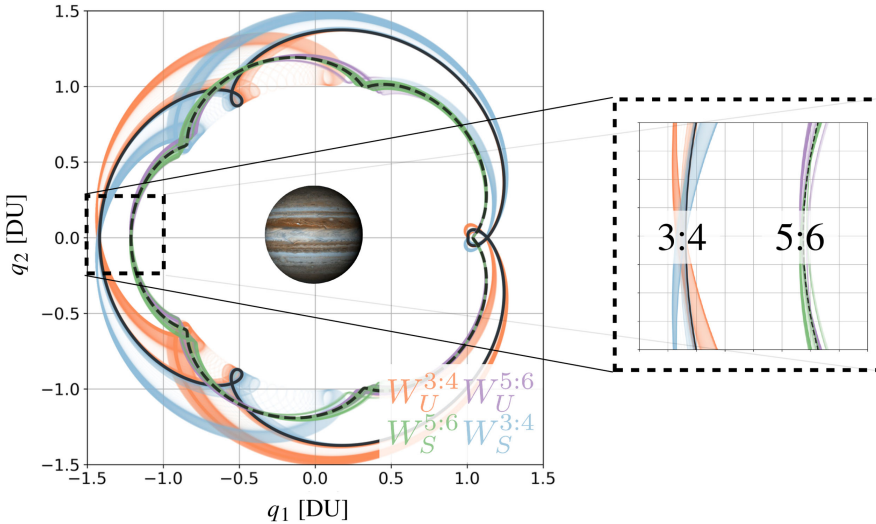


**Fig. 3** The 3:4 and 5:6 resonant orbits with corresponding unstable and stable manifolds.

between the different realms of this model and therefore can also be used to construct low-energy spacecraft trajectories. They can also be classified as stable and unstable: a stable invariant manifold encompasses all points that converge to a limit set as time progresses toward infinity; conversely, an unstable manifold comprises all points that converge to the same limit set as time retrogresses toward negative infinity. We denote the unstable invariant manifold corresponding to a periodic orbit  $\gamma$  by  $W_U^\gamma$ . This is the set  $\mathcal{Z}$  such that  $z(t) \rightarrow \gamma$  as  $t \rightarrow -\infty$ ,  $\forall z \in \mathcal{Z}$ . Conversely,  $W_S^\gamma$  represents the stable invariant manifold, and comprises the set  $\mathcal{Z}$  such that  $z(t) \rightarrow \gamma$  as  $t \rightarrow \infty$ ,  $\forall z \in \mathcal{Z}$ . A spacecraft originally on  $\gamma$  will shadow  $W_S^\gamma$  when perturbed in the direction of the stable eigenvector of the monodromy matrix corresponding to  $\gamma$ , and will shadow  $W_U^\gamma$  when perturbed in the direction of the unstable eigenvector. Invariant manifolds share the same Jacobi integral as the periodic orbits to which they are associated. The invariant manifolds associated with the 3:4 and 5:6 resonant orbits in the Jupiter-Europa system are shown in Fig. 3. The 3:4 resonant orbit ( $C_{3:4} = 2.995$ ) is shown here in solid black, and the 5:6 resonant orbit ( $C_{3:4} = 3.005$ ) is shown in dashed black. The 3:4 unstable invariant manifold  $W_U^{3:4}$  is shown in orange, and the corresponding stable invariant manifold  $W_S^{3:4}$  is in blue. Similarly, the 5:6 unstable invariant manifold  $W_U^{5:6}$  is shown in purple, and the corresponding stable invariant manifold  $W_S^{5:6}$  is in green.

The invariant manifolds describe the local dynamics in the neighborhood of the periodic orbits and provide a global template for LT trajectories. As mentioned before, previous studies have shown that optimization algorithms applied to minimum-fuel problems and without explicit prior knowledge of the underlying DS qualitatively converge to locally optimal solutions that align themselves with these structures. Anderson and Lo [22] extended the work of Lo [50] to investigate a minimum-fuel LT moon tour in the Jupiter-Europa CR3BP, originally developed by Lam et al. [51], using the trajectory design tool Mystic [52]. They discovered that the numerical optimal trajectories indeed appear to shadow the invariant manifolds of resonant orbits. The main purpose of this paper is to further extend Anderson and Lo's work beyond qualitative understanding to a quantitative one, as well as to study robust trajectories and their dependence on the underlying DS. We aim to compare the behavior of robust and nonrobust trajectories in relation to these structures. Having knowledge of the relationship of the robust solutions to the DS can be useful in developing good initial guesses and efficient algorithms for the global design of robust optimal LT trajectories.

## IV. Analysis Methods

### A. Poincaré Surface of Sections

Poincaré return maps, or simply Poincaré maps, are an effective tool for analyzing rotational flows such as periodic or quasi-periodic

orbits, or even flow in the vicinity of a periodic orbit, and can therefore be used to investigate the trajectories as well as pertinent invariant manifolds [48,49]. We consider a point  $x \in \mathcal{S}$  on the surface  $\mathcal{S}$ , which we evolve in time according to the governing dynamical equations until it intersects  $\mathcal{S}$  again transversely. We denote the intersection of the point  $x$  with  $\mathcal{S}$  as  $\mathcal{P}(x)$ . Therefore,  $\mathcal{P}(x)$  represents the first return of the trajectory to  $\mathcal{S}$ ,  $\mathcal{P}^2(x)$  represents the second return of the trajectory to  $\mathcal{S}$ , and so on. We can continue to evolve  $x$  in time and record its state after every intersection with  $\mathcal{S}$ , and by doing so, we effectively reduce the global orbit structure governed by differential equations to a discrete-time dynamical system given by the map  $\mathcal{P}$ . A Poincaré map can therefore be mathematically described by  $\mathcal{P}: \mathcal{S} \rightarrow \mathcal{S}$ , where  $\mathcal{S}$  is referred to as the Poincaré surface of section, or simply Poincaré section (see Fig. 4a for a visual representation). The forward-in-time integrated map of  $x$  is represented by  $\mathcal{P}(x)$  and is indicated with a circle. Conversely, the backward-in-time integrated map of  $x$  is represented by  $\mathcal{P}^{-1}(x)$  and is indicated with a square. The forward-integrated map coincides with the backward-integrated map of a trajectory only if the point  $x$  belongs to a periodic orbit. If a trajectory is (sufficiently) planar, the map  $\mathcal{P}$  provides sufficient information to fully characterize the trajectory.

An example Poincaré section is shown in Fig. 4. Every puncture point on a given Poincaré section possesses the same Jacobi integral. Puncture points corresponding to the evolution of the forward integrated nonrobust solution  $\mathcal{P}(x_{nr})$  and robust solution  $\mathcal{P}(x_r)$  are denoted by black and blue circles, respectively, which were computed by mapping points along the state forward in time without thrust until it intersected  $\mathcal{S}$ . Similarly, puncture points corresponding to the evolution of the backward integrated nonrobust  $\mathcal{P}^{-1}(x_{nr})$  and robust trajectory  $\mathcal{P}^{-1}(x_r)$  are denoted by black and blue squares. In this study, we only record the first puncture point for trajectories, discarding the subsequent ones.

The puncture points corresponding to the stable and unstable invariant manifolds for the relevant resonant orbits are an important part of the analysis in this study. In our study, the sets containing these puncture points are labeled as  $W_i^\gamma$ , where the superscript  $\gamma$  allows us to discern what type of periodic orbit we are referring to and the subscript  $i$  allows us to discern the stability of the invariant manifolds. To compute the invariant manifold puncture points, one begins by considering perturbations parallel (and antiparallel) to the eigenvectors of the monodromy matrix, which are then propagated forward (if unstable) or backward (if stable) in time until their first intersection with  $\mathcal{S}$ . The states of these puncture points are recorded and plotted using a coordinate system of choice (e.g.,  $q_1 - \dot{q}_1$ ). In this study, we consider a range of perturbation from  $[1 \times 10^{-6}, 3 \times 10^{-1}]$  (in nondimensional units) both parallel to and antiparallel to the eigenvectors of the monodromy matrix, which are then

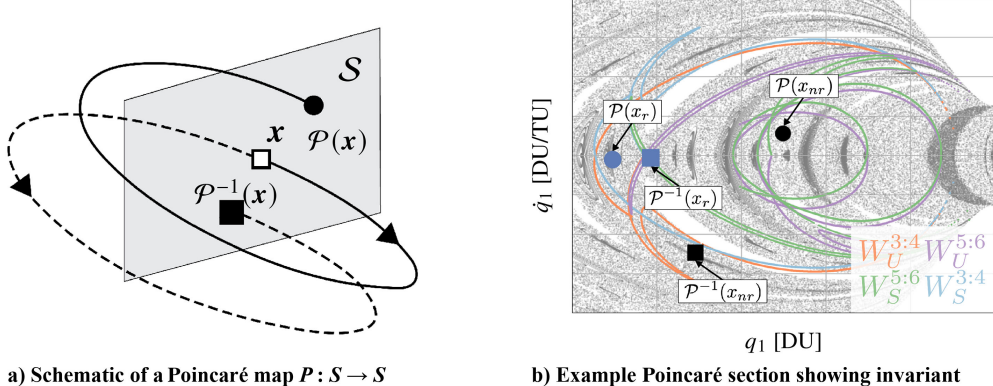


Fig. 4 Schematic of a Poincaré map along with an example Poincaré section.

propagated until their first intersection with  $\mathcal{S}$ . Alternatively, one could compute the invariant manifold puncture points by considering a state on  $\gamma$  with a fixed perturbation magnitude and capturing multiple intersections with  $\mathcal{S}$ . Using a range of perturbation magnitudes and recording the first intersection is equivalent to applying a fixed perturbation magnitude and recording multiple intersections, as long as the perturbations are initialized within an acceptable range where the linear approximation of the manifolds is realized.  $W_U^{3:4}$  represents the intersection of the unstable manifold of the 3:4 resonant orbit (orange),  $W_S^{3:4}$  represents the intersection of the stable manifold of the 3:4 resonant orbit (blue),  $W_U^{5:6}$  represents the intersection of the unstable manifold of the 5:6 resonant orbit (purple), and  $W_S^{5:6}$  represents the intersection of the stable manifold of the 5:6 resonant orbit (green). Approximately 10,000 puncture points are computed for each invariant manifold in the subsequent analysis.

The background points (gray) are computed by first considering points on a uniform grid on the  $x$ -axis on  $\mathcal{S}$  and then integrating these points forward in time until they intersect the surface a number of times. The number of points retained for subsequent analysis is largely problem dependent but should be chosen such that a sufficiently detailed visual representation of the global dynamical flow template is visible. In this study, the background points are computed by considering 10,000 points on an equally spaced grid on the  $x$ -axis on  $\mathcal{S}$  and integrating forward in time until they intersect the surface 10 times. The first five puncture points were discarded to remove the distortion of the grid during integration, and the remaining puncture points were recorded. The number of intersections being retained was arbitrarily chosen, but for the context of this research, this choice does not impact the results since the background points are only for visual purposes and do not affect any of the subsequent analyses. Note that 50,000 points were recorded for the background points in total.

## B. Jacobi Integral of Low-Thrust Trajectories

The Jacobi integral of a low-thrust trajectory changes whenever the spacecraft executes a maneuver, so we need to ensure that the invariant manifolds, to which we are comparing the trajectory puncture points, possess the same Jacobi integral. To do so, we first uniformly discretize the Jacobi integral interval between the initial orbit (3:4 resonant orbit,  $C_{3:4} = 2.995$ ) and the final orbit (5:6 resonant orbit,  $C_{5:6} = 3.005$ ) with steps of 0.001, and for each point in that interval, we compute the resonant orbit (and their invariant manifolds) possessing that Jacobi integral. We store the information in a look-up table, which will be used later in the subsequent analysis. Ideally, we would like to compare every point on a trajectory with the pertinent resonant orbits at those energy levels, but doing so would be numerically intractable. Our approach closely parallels the methodology presented by Anderson and Lo [22]. Figure 5 illustrates the resonant orbits used in this analysis. To compute the resonant orbits, we use the initial conditions from the database developed by Restrepo and Russell [53]. For each resonant orbit shown, their invariant manifolds are also computed (not shown in the figure), and approximately 10,000 puncture points are recorded for each invariant manifold.

Figure 6 illustrates the Jacobi integral associated with a representative nonrobust solution. As the spacecraft's trajectory evolves in time, its Jacobi integral undergoes a change every time the spacecraft executes a maneuver. We begin by filtering points along the trajectory possessing a Jacobi integral close to that of one of the periodic orbits in our look-up table (in our case, we set this threshold to  $1 \times 10^{-6}$ ). For example, the first point corresponds to a Jacobi integral of  $\approx 2.995$ . So, we compare its forward and backward integrated trajectory with the 3:4 and 5:6 resonant orbit invariant manifolds possessing the same energy, shown with a solid line and a dashed black line, respectively, in each subfigure. The remaining orbits in the dictionary are shown in the background in gray. The corresponding Poincaré section  $\mathcal{S}$  with the relevant puncture points

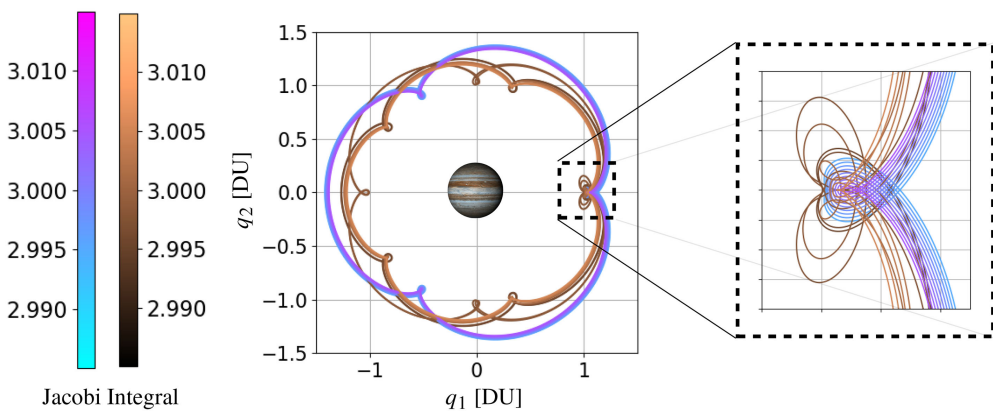
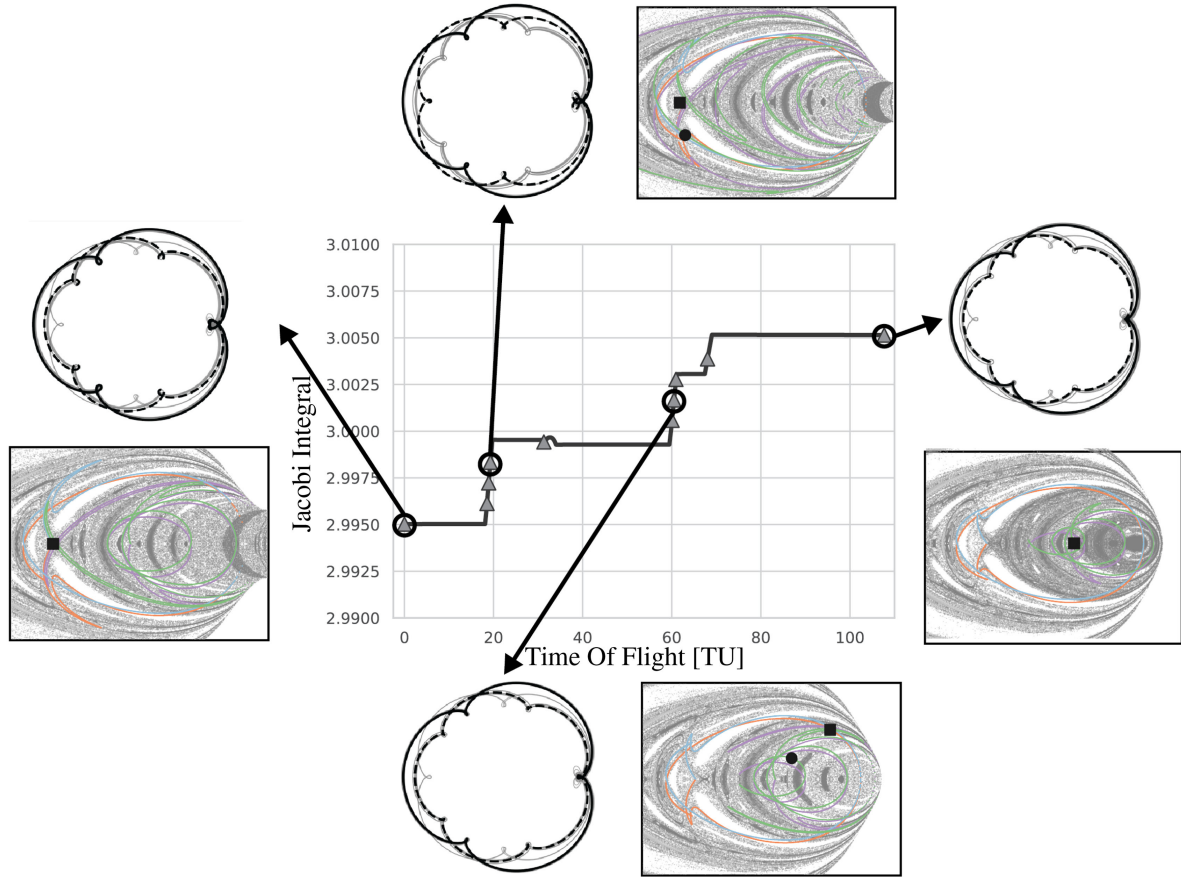


Fig. 5 Family of 3:4 and 5:6 resonant orbits colored by Jacobi integral levels.



**Fig. 6** Jacobi integral for a nonrobust solution with trajectory points and corresponding Poincaré section.

is also shown in the subfigure. From each filtered subset, we randomly select a point and integrate it forward and backward in time under natural dynamics until they intersect with the Poincaré section  $\mathcal{S}$  to produce  $\mathcal{P}(\mathbf{x})$  and  $\mathcal{P}^{-1}(\mathbf{x})$ , respectively. We compare these puncture points to those of the invariant manifolds of the resonant orbits with the same Jacobi integral, ensuring that all points on a given Poincaré section possess the same energy.

### C. Distance Metrics on Poincaré Surface of Sections

By the process outlined above, it is possible to visualize the evolution of the trajectory puncture points on the Poincaré section  $\mathcal{S}$ , and compare them to the invariant manifolds of the pertinent resonant orbits. However, in addition to qualitatively visualizing the solutions, we also aim to understand quantitatively if there is a difference in the behavior of the solutions with respect to the invariant manifolds, and in that regard, we introduce two distance metrics on  $\mathcal{S}$  (see Fig. 7 for a schematic).

#### 1. Orthogonal Distance to the Nearest Invariant Manifold

First, we introduce a distance metric to quantify the degree to which a given trajectory leverages the underlying invariant manifolds in our problem. We define  $d_T^S(x^{\mathcal{P}}, \mathcal{W})$  as the shortest orthogonal distance between  $x^{\mathcal{P}}$ , a trajectory puncture point, and  $\mathcal{W}$ , a set of invariant manifold puncture points on  $\mathcal{S}$ . For example,  $d_T^S(\mathcal{P}(x_{nr}), W_U^{3:4})$  represents the shortest distance between the nonrobust forward-integrated trajectory puncture point  $\mathcal{P}(x_{nr})$  and the unstable manifold puncture points of the 3:4 resonant orbit  $W_U^{3:4}$ . We denote the shortest distance from a given trajectory puncture point  $x^{\mathcal{P}}$  to *any* of the invariant manifolds as

$$\hat{d}_T^S(x^{\mathcal{P}}) \equiv \min_{W_i^{\gamma}} d_T^S(x^{\mathcal{P}}, W_i^{\gamma}) \quad (17)$$

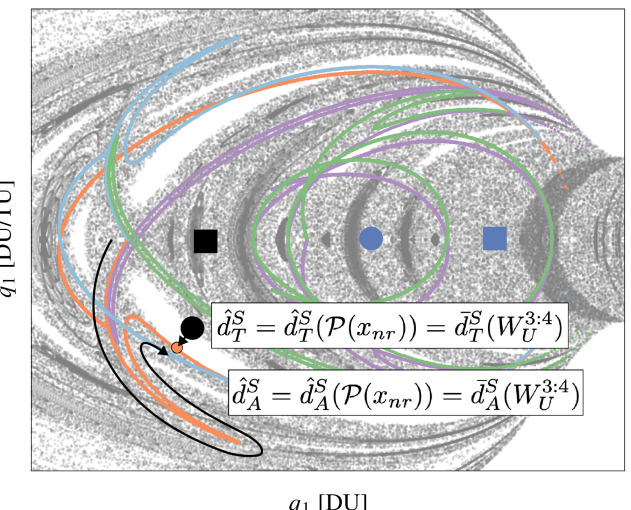


**Fig. 7** Example Poincaré section illustrating distance metrics and their relationship to invariant manifolds.

where  $x^{\mathcal{P}}$  may refer to either the forward-integrated trajectory point  $\mathcal{P}(\mathbf{x})$  or the backward-integrated trajectory point  $\mathcal{P}^{-1}(\mathbf{x})$ . Conversely, we denote the shortest distance from a given invariant manifold  $W_i^{\gamma}$  of a resonant orbit to any of the trajectory puncture points as

$$\bar{d}_T^S(W_i^{\gamma}) \equiv \min_{x^{\mathcal{P}} \in \{\mathcal{P}(\mathbf{x}), \mathcal{P}^{-1}(\mathbf{x})\}} d_T^S(x^{\mathcal{P}}, W_i^{\gamma}) \quad (18)$$

where  $W_i^{\gamma}$  may refer to  $W_U^{3:4}$ ,  $W_S^{3:4}$ ,  $W_U^{5:6}$ , or  $W_S^{5:6}$ .

## 2. Distance Along the Nearest Invariant Manifold

We introduce an additional distance metric to quantify the distance a trajectory must traverse along an invariant manifold to reach the nearest resonant orbit. Let  $w \in \mathcal{W}$  represent a point in the set containing the invariant manifold puncture points  $\mathcal{W}$ . The arc length between  $w$  and the separatrix, measured along the invariant manifold, quantifies the distance the spacecraft will have to coast to reach the corresponding resonant orbit. We denote this arc length as  $d_A^S(x^P, w)$ . Of particular interest is the distance along the invariant manifold of an invariant manifold puncture point that is orthogonally closest to the trajectory puncture point, i.e., the invariant manifold puncture points that yields  $\hat{d}_T^S(x^P)$ , which we denote as

$$\hat{d}_T^S(x^P) \equiv d_A^S(x^P, w) \text{ s.t. } w = \arg \min_{W_j^i} d_T^S(x^P, W_j^i) \quad (19)$$

Conversely, we denote the arc length along a given invariant manifold puncture point set  $W_i^Y$  from the point in the invariant manifold puncture point set closest to the trajectory puncture points as

$$\bar{d}_A^S(W_i^Y) \equiv \min_{x^P \in \{\mathcal{P}(x), \mathcal{P}^{-1}(x)\}} d_A^S(x^P, w) \text{ s.t. } w = \arg \min_{W_j^i} d_T^S(x^P, W_j^i) \quad (20)$$

The arc length  $L$  along the invariant manifolds is computed as the cumulative Euclidean distance between consecutive points along the manifold trajectory in the specified coordinates on  $S$ , given by

$$L = \sum_i \sqrt{\Delta q_i^2 + \Delta \dot{q}_i^2} \quad (21)$$

where  $\Delta q_i$  and  $\Delta \dot{q}_i$  represent the differences in position and velocity coordinates between consecutive points on the arc. To ensure the accuracy of this approximation, a dense mapping of the invariant manifold on  $S$  is necessary.

Finally, we introduce the following definitions to represent the minimum distance between the invariant manifold puncture points and the trajectory puncture points, irrespective of whether they were forward-integrated or backward-integrated in time:

$$\hat{d}_T^S \equiv \min\{d_T^S(\mathcal{P}(x)), d_T^S(\mathcal{P}^{-1}(x))\} \quad (22)$$

$$\hat{d}_A^S \equiv \min\{d_A^S(\mathcal{P}(x)), d_A^S(\mathcal{P}^{-1}(x))\} \quad (23)$$

The metric  $\hat{d}_T^S$  provides a measure of how far, at any given time, the trajectory is from *any* of the invariant manifolds. By recording this distance at multiple time snapshots across different solutions, we can assess how effectively different solution families exploit the underlying invariant manifolds for minimum-fuel transfers, thereby providing insights into the role of DS in the optimization process. On the other hand, the metric  $\hat{d}_A^S$  quantifies the distance the spacecraft will have to coast to reach the nearest resonant orbit at any given energy level. This distance allows us to elucidate how fast the trajectory can coast along the nearest invariant manifold and, thereby, provides deeper insights into how these trajectories are leveraging these structures.

## V. Results and Discussion

### A. Numerical Experimental Design

In this section, we present the implementation details about the numerical experiments. We consider a minimum fuel transfer between a 3:4 resonant orbit and a 5:6 resonant orbit in the Jupiter–Europa system, characterized by the nondimensional gravitational parameter  $\mu$  equal to  $2.52856 \times 10^{-5}$ . The boundary conditions for the optimal control problem are shown in Fig. 8, where the initial boundary condition is given by  $[-0.37322, 1.20130, 0.0, 0.33434, 0.25594, 0.0]$ , and the terminal boundary condition is given by  $[-0.68463, -0.96387, 0.0, -0.20325, 0.20764, 0.0]$ ,

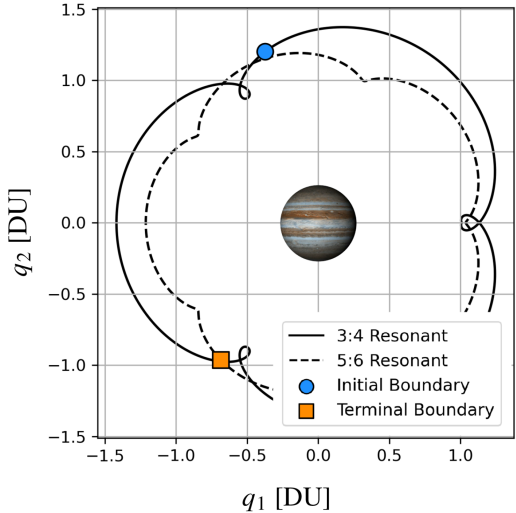


**Fig. 8** Boundary conditions for the LT transfer.

**Table 2** Spacecraft parameters

Parameter	Value
Number of segments	50
$I_{SP}$ , s	1000.0
Thrust acceleration, m/s <sup>2</sup>	0.001
Dry mass, kg	700.0
Fuel mass, kg	300.0

with the position and velocity components written in nondimensional units. In the Jupiter–Europa CR3BP model, 1 DU = 670,900.0 km, 1 TU = 48,822.8 s, and 1 VU = 13.7 km/s.

The spacecraft parameters are summarized in Table 2. The spacecraft has a dry mass of 700.0 kg and an initial fuel mass of 300.0 kg. It operates under a constant specific impulse propulsion model with a specific impulse of 1000.0 s and a maximum thrust acceleration of 0.001 m/s<sup>2</sup>. We use a forward–backward control transcription characterized by 50 segments. Numerical tolerances for matchpoint constraint violations are defined as  $1 \times 10^{-6}$  DU for position and  $1 \times 10^{-6}$  VU for velocity, and  $1 \times 10^{-3}$  kg for mass. Temporal bounds include a shooting time range of  $[0.0, 90.0]$  TU, an initial coast time range of  $[0.0, 25.46898]$  TU, and a final coast time range of  $[0.0, 38.14625]$  TU, where the upper bounds on the coast times correspond to the orbital period of the 3:4 resonant orbit and the orbital period of the 5:6 resonant orbit, respectively.

### B. Qualitative Analysis

To differentiate between robust and nonrobust solutions, we analyze, both qualitatively and quantitatively, snapshots across the evolution of a specific solution and compare the robust puncture points with their nonrobust counterparts. Intuitively, one might expect robust solutions to be less efficient than nonrobust ones, leading to larger deviations from the underlying invariant manifolds, and this is certainly true for the solutions shown in Fig. 9, which corresponds to an optimal nonrobust solution and an optimal robust solution, where  $\tau_1$  coincides with the beginning of the 44th control segment, and  $\Delta\tau = 2.5$  TU. Looking at the temporal evolution of the Jacobi integral over time, we notice that the rate of change of the Jacobi integral of the nonrobust solution is mostly nonnegative, while that of the robust solution exhibits more frequent fluctuations. A majority of robust solutions display similar behavior, and this observation aligns with our hypothesis that robust solutions can sometimes undergo inefficient maneuvers to attain feasibility.

The evolution of the puncture points on  $S$  for both solutions is shown in Fig. 10. The robust trajectory puncture points follow a different path than the nonrobust puncture points, but both seem to be relatively well-aligned with the invariant manifold puncture

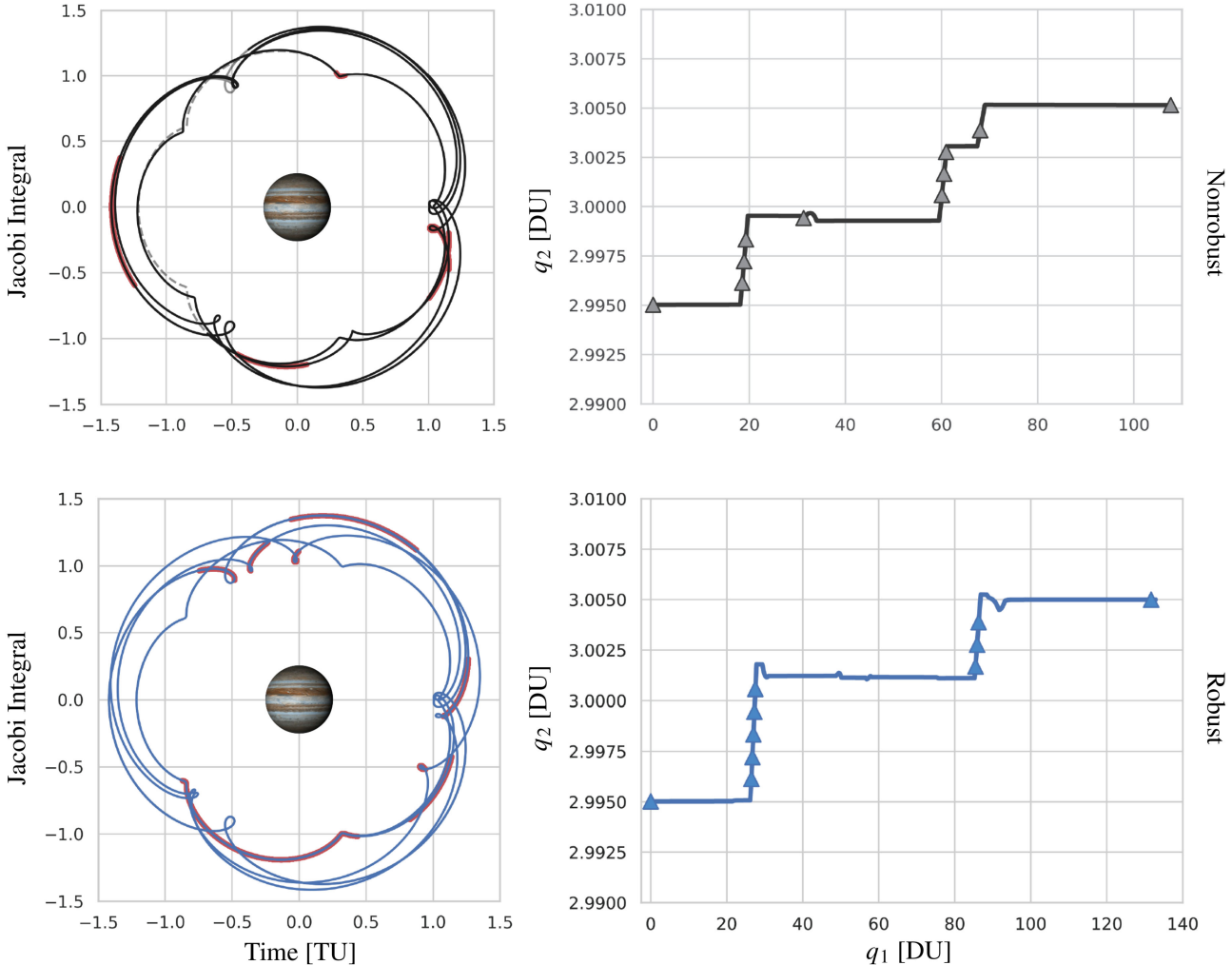


**Fig. 9 Representative nonrobust and robust solutions with thrust arcs and Jacobi integrals.**

points. We now analyze the nonrobust solution in more detail. As one would expect, both  $\mathcal{P}(\mathbf{x}_{\text{nr}})$  and  $\mathcal{P}^{-1}(\mathbf{x}_{\text{nr}})$  begin at the 3:4 separatrix (frame I).  $\mathcal{P}(\mathbf{x}_{\text{nr}})$  remains close to this point (frames II and III), before transitioning to  $W_U^{3:4}$ , which it flows along (frames IV and V). Then, it transfers between invariant manifolds (frames VI–IX), maintaining close proximity to both  $W_U^{5:6}$  and  $W_S^{5:6}$ , until it eventually reaches the 5:6 separatrix (frame X). On the other hand,  $\mathcal{P}^{-1}(\mathbf{x}_{\text{nr}})$  immediately latches onto  $W_S^{3:4}$  which it flows along (frames II and III), before it returns back to the separatrix (frame IV and V). Then, it transitions to  $W_S^{5:6}$ , which it flows along (frames VI–IX) until it reaches the 5:6 separatrix (frame X). Between frames I and V, the spacecraft has optimized its thrust to move  $\mathcal{P}(\mathbf{x}_{\text{nr}})$  along  $W_U^{3:4}$  while aligning  $\mathcal{P}^{-1}(\mathbf{x}_{\text{nr}})$  for the subsequent transition into  $W_S^{5:6}$ . Then, between frames VI and X, the thrust is used to transition  $\mathcal{P}^{-1}(\mathbf{x}_{\text{nr}})$  along  $W_S^{5:6}$ , while transferring  $\mathcal{P}(\mathbf{x}_{\text{nr}})$  between different invariant manifolds until they settle at the 5:6 separatrix.

Moving on to the robust solution, naturally, both  $\mathcal{P}(\mathbf{x}_r)$  and  $\mathcal{P}^{-1}(\mathbf{x}_r)$  begin at the 3:4 separatrix (frame I).  $\mathcal{P}(\mathbf{x}_r)$  aligns itself with the  $W_U^{3:4}$ , which it flows along (frames II–VI). In the subsequent frames, it “oscillates” about the 5:6 separatrix (frames VII–IX) before eventually settling at the separatrix (frame X).  $\mathcal{P}^{-1}(\mathbf{x}_r)$ , on the other hand, follows a rather interesting path. We do not see any major change during the initial frames (frames I–VI). Then, we see it abruptly transition to  $W_S^{5:6}$  (frame VII), which it flows along (frames VII–IX) until it reaches the 5:6 separatrix (frame X). Between frames I and VI, the spacecraft has optimized its thrust to first move  $\mathcal{P}(\mathbf{x}_r)$  along  $W_U^{3:4}$  while making minimal changes to  $\mathcal{P}^{-1}(\mathbf{x}_r)$ , and then, in frame VII, to move both  $\mathcal{P}(\mathbf{x}_r)$  and  $\mathcal{P}^{-1}(\mathbf{x}_r)$  over to  $W_S^{5:6}$ . Finally, between frames VII and X, the thrust

is mostly used to move  $\mathcal{P}(\mathbf{x}_r)$  and  $\mathcal{P}^{-1}(\mathbf{x}_r)$  along  $W_S^{5:6}$  (frames VII–IX) until they settle at the 5:6 separatrix.

### C. Quantitative Analysis

From the analysis of this solution, we observe that both robust and nonrobust trajectories exhibit certain qualitative similarities and differences. Notably, the robust solution appears to flow along the invariant manifolds, whereas the nonrobust solution appears to transfer between the invariant manifolds (e.g., frames VI–IX). However, generalizing the relationship between trajectory and invariant manifold puncture points based solely on visual inspection of a single solution pair is difficult. The observed trend in the solutions shown in Sec. V.B may be specific to this particular pair and may not be representative of the entire solution family. Further, it is also important to note that the snapshots are nonuniform in time. As a result, we often notice large “jumps” in the path of the trajectory puncture points (e.g., frames V and VI for the nonrobust solution; frames VI and VII for the robust solution). So, instead, by analyzing a collection of solutions, we hope to be able to “average out” the nonuniformity in time to globally characterize the solution trends in relation to the invariant manifolds.

To assess whether the observed trend persists across solution families, we first generate a set of feasible and optimal solutions for both the nonrobust and robust problems, varying the parameters  $\tau_1$  and  $\Delta\tau$ . The optimal solutions, a subset of the feasible solutions, comprise the solutions that meet the optimizer’s optimality criteria, specifically those exiting with SNOPT Exit Info 1 [54]. The number of solutions and puncture points used in this study is presented in Table 3.

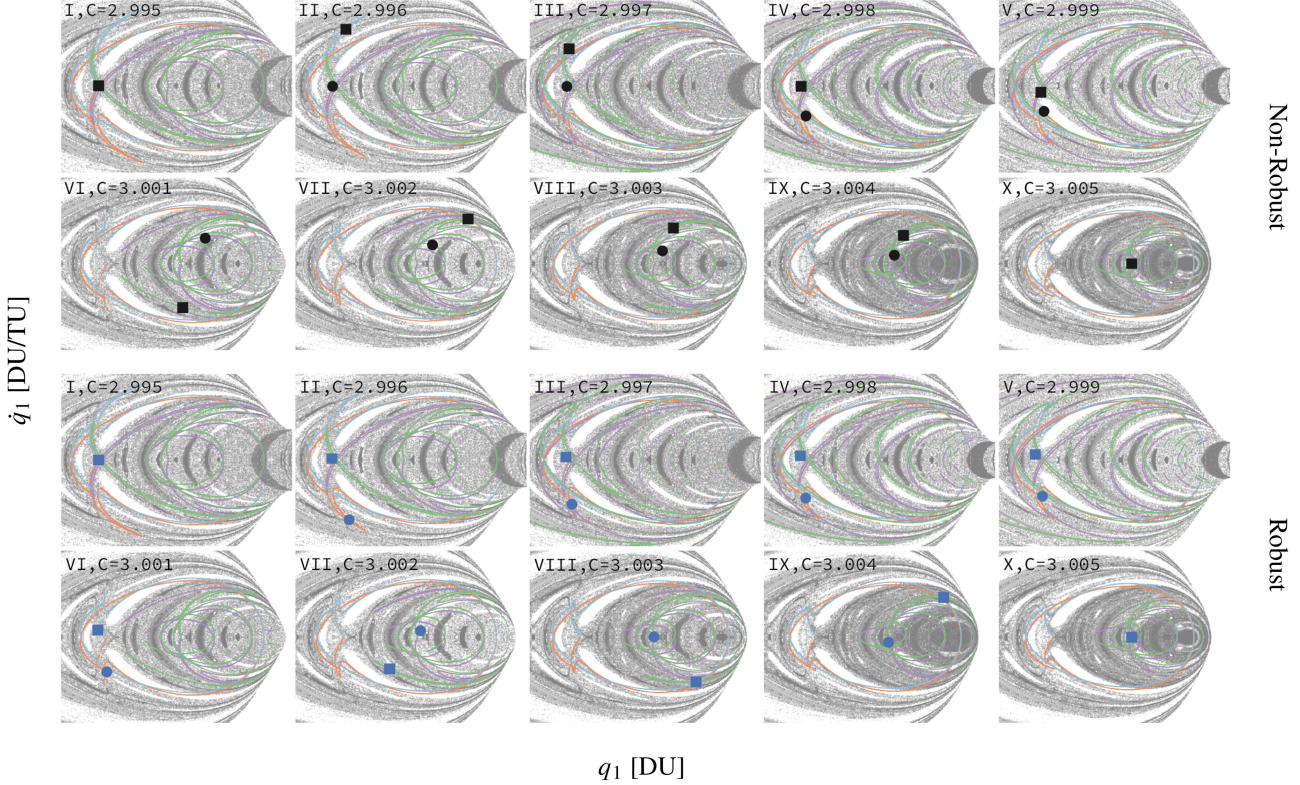


Fig. 10 Snapshots showing temporal evolution of puncture points on  $\mathcal{S}$  for nonrobust (black) and robust (blue) solutions.

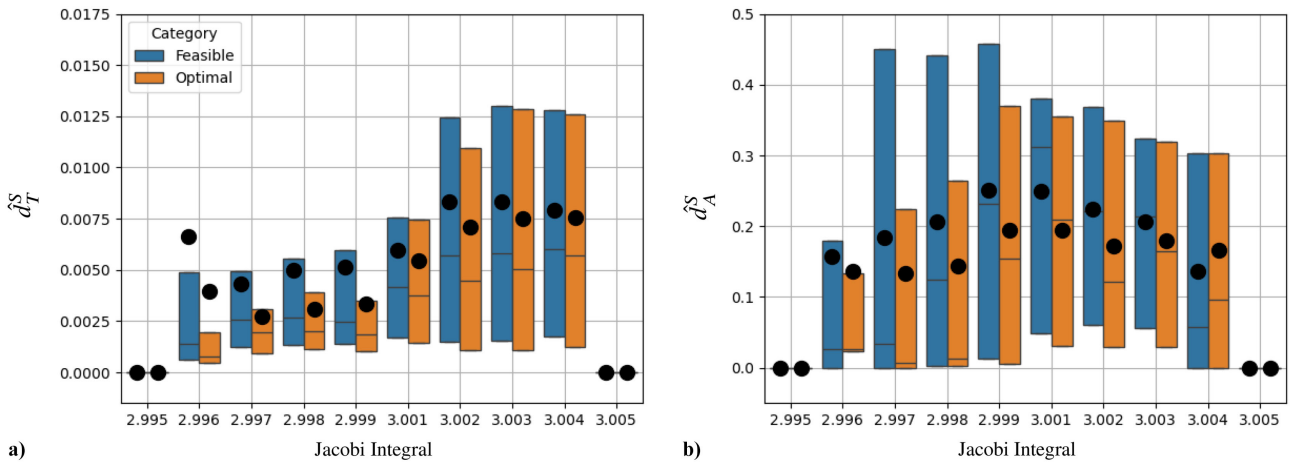
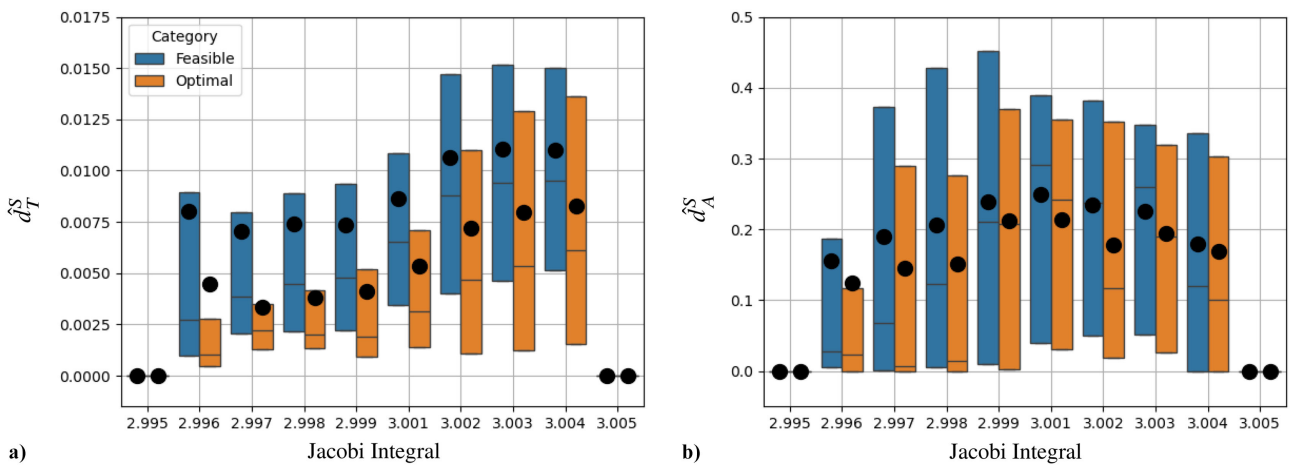
Table 3 Number of solutions and punctures

	Nonrobust		Robust	
	Feasible	Optimal	Feasible	Optimal
Number of solutions	21,455	9,393	6,789	958
$\Delta\tau$ (TU)	0.5	1,051	171	
	1.0	932	140	
	2.5	1,016	156	
	5.0	1,002	153	
	10.0	969	133	
	15.0	951	121	
	30.0	868	84	
$\tau_1$	Forward shooting arc		2,850	224
	Backward shooting arc		3,939	734
Number of punctures	168,722	143,890	65,895	17,202
$\Delta\tau$ (TU)	0.5	10,068	3,071	
	1.0	8,902	2,399	
	2.5	9,918	2,914	
	5.0	9,702	2,753	
	10.0	9,459	2,433	
	15.0	9,275	2,104	
	30.0	8,571	1,501	
$\tau_1$	Forward shooting arc		33,014	4,300
	Backward shooting arc		32,881	12,902

In this section, we provide a detailed quantitative analysis to complement the qualitative observations. Using the distance metrics discussed in Sec. IV.C, we aim to examine the statistical differences between the nonrobust and robust solutions relative to the invariant manifolds. We begin by computing  $\hat{d}_T^S$  and  $\hat{d}_A^S$  for the nonrobust and the robust solutions and then compare the statistics between the feasible solutions and the optimal solutions in each category (Figs. 11, 12). The circles represent the mean, the horizontal lines represent the median, and the colored bars represent the interquartile range.

As expected,  $\hat{d}_T^S$  is zero at the first and the last frames since the trajectory puncture points at those frames coincide with the separatrices of the 3:4 and 5:6 resonant orbits, respectively, and therefore

the corresponding  $\hat{d}_T^S$  should be exactly zero. The same idea applies for  $\hat{d}_A^S$ . As we progress through the energy levels, the mean  $\hat{d}_T^S$  increases for both solution categories. Since the transfer is from a 3:4 resonant orbit farther from Europa to a 5:6 resonant orbit closer to Europa (see Fig. 5), we anticipate greater sensitivity in the solutions during the later energy levels, which correspond to points along the trajectory closer to Europa, and therefore subject to dynamics highly sensitive to perturbations. Accordingly, we expect the puncture points corresponding to the later energy levels to show less reliance on the invariant manifolds compared to those at earlier levels, as the dynamics may be too chaotic for the optimizer to leverage the invariant manifolds effectively for a finite horizon minimum-fuel transfer. This expectation is confirmed by the higher

Fig. 11 The  $\hat{d}_T^S$  and  $\hat{d}_A^S$  for nonrobust solutions.Fig. 12 The  $\hat{d}_T^S$  and  $\hat{d}_A^S$  for robust solutions with varying  $\Delta\tau$  and  $\tau_1$ .

mean  $\hat{d}_T^S$  observed at the later energy levels relative to the earlier ones. Throughout the analysis, however, the optimal solutions consistently remain closer to the invariant manifolds on average compared to the feasible solutions, a trend that persists across energy levels and solution categories, suggesting that closer alignment with the invariant manifolds is necessary to achieve optimality. Robust feasible solutions exhibit a slightly higher  $\hat{d}_T^S$  compared to the nonrobust solutions, while the optimal set of robust solutions demonstrates a substantial decrease in  $\hat{d}_T^S$ , bringing it nearly in line with those for the nonrobust solutions.

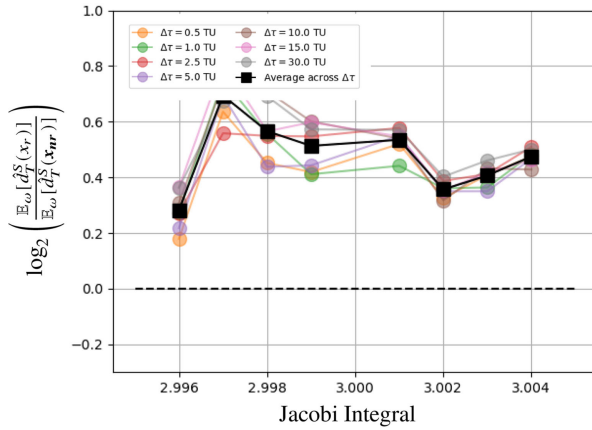
The statistics for  $\hat{d}_A^S$  show a similar trend between the feasible and optimal solutions, for both the nonrobust and the robust solution categories. For both solution categories, the  $\hat{d}_A^S$  remain relatively small during the initial energy levels, which increases as we progress through the energy levels, before decreasing again at the later energy levels. Given that the solutions involve transfers between resonant orbits, we expect  $\hat{d}_A^S$  to remain small when the trajectory is in proximity to the resonant orbits, which justifies the lower  $\hat{d}_A^S$  in the earlier and the later energy levels when the spacecraft is departing the 3:4 resonant orbit and entering the 5:6 resonant orbit, respectively, and higher in between.

To compare the robust solutions with the nonrobust solutions as we vary  $\tau_1$  and  $\Delta\tau$ , we calculate the fold change in the mean distance metrics for the robust solutions relative to their nonrobust counterparts. To visualize this change, we use the  $\log_2$  of the fold change as a metric, where a value of zero indicates that the distance metrics for the robust solutions and the nonrobust solutions are the same, a positive value indicates an increase, and a negative value indicates a decrease. We remove the first and last energy levels from the

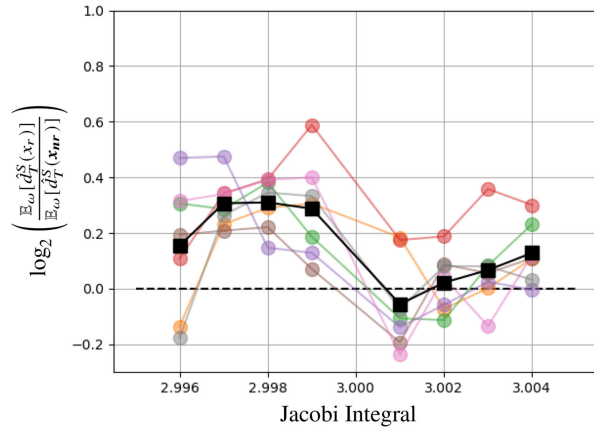
subsequent analysis since they correspond to the separatrices of the 3:4 and 5:6 resonant orbits, respectively. We begin by analyzing the solutions grouped according to  $\Delta\tau$ , noting that each group contains solutions with varying  $\tau_1$ . Subsequently, we analyze the solutions by grouping them according to  $\tau_1$ , where each group similarly includes solutions with different  $\Delta\tau$ .

### 1. Dependence on $\Delta\tau$

In this section, we explore how the relationship to the invariant manifolds changes as we vary  $\Delta\tau$  for the robust solutions. If we consider the entire feasible solution set, the mean  $\hat{d}_T^S$  across  $\Delta\tau$  for the robust solutions is greater than that for the nonrobust solutions (Fig. 13a). However, if we focus on the optimal solution subset, the mean  $\hat{d}_T^S$  across  $\Delta\tau$  for the robust solutions significantly diminishes and appears to resemble the nonrobust solutions more closely, especially toward the later energy levels (Fig. 13b). We even notice some robust solution categories exhibiting closer alignment to the invariant manifolds than the nonrobust solutions. This observation is particularly significant because, as we have seen before, the solutions rely less on invariant manifolds at the later energy levels. The fact that robust solutions exhibit comparable, and in some cases stronger, alignment with these invariant manifolds at the later energy levels, relative to the nonrobust solutions, suggests an important insight. Despite the chaotic dynamics, robust optimal solutions are still effectively leveraging the invariant manifolds, almost as closely as the nonrobust solutions. The results also suggest that while feasible robust solutions may generally deviate from the invariant manifolds, the optimal ones tend to shadow the invariant manifolds almost as closely as the nonrobust optimal solutions.



a) Feasible solutions



b) Optimal solutions

Fig. 13 Fold change in  $\hat{d}_T^S$  for robust solutions with varying  $\Delta\tau$  relative to nonrobust solutions.

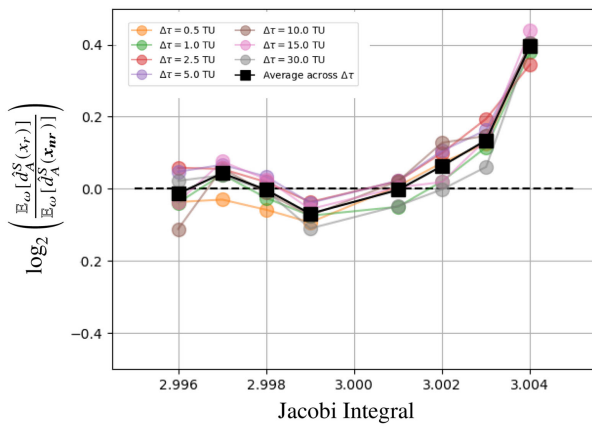
An interesting trend emerges in the second distance metric. During the initial energy levels, the robust optimal solutions exhibit a larger mean  $\hat{d}_A^S$  across  $\Delta\tau$  relative to the nonrobust optimal solutions (Fig. 14b), particularly when compared to the overall feasible solution set (Fig. 14a). At the initial energy levels, the mean  $\hat{d}_A^S$  across  $\Delta\tau$  for the robust and nonrobust feasible solutions are similar. However, as we progress through the energy levels, the ratio decreases slightly before increasing. If we focus only on the optimal solutions subset, we find that this distance metric for the robust solutions is lower at the first and last frames but shows a modest increase in between. As explained before, this is the behavior we expect since solutions are typically closer to resonant orbits during departure from the 3:4 resonant orbit (i.e., the early frames) and arrival at the 5:6 resonant orbit (i.e., the later frames). The behavior of the robust optimal solutions observed in this distance metric suggests strong alignment with this hypothesis.

Compared to nonrobust solutions, robust solutions exhibit larger deviations from the invariant manifolds at earlier energy levels and smaller deviations at later energy levels (see Fig. 13). This behavior reflects the compensatory mechanisms employed by robust solutions to balance feasibility with disruptions in the control authority. The dependence on  $\Delta\tau$  becomes particularly significant at the later energy levels (e.g., Jacobi Integral  $>3.000$ ), as the solutions approach the terminal phases of the transfer. At these later energy levels, robust solutions generally exhibit increased deviations from the invariant manifolds as  $\Delta\tau$  increases. However, a notable exception occurs for the case of  $\Delta\tau = 2.5$  TU, which stands out as an outlier and does not conform to the observed trend. In contrast, at lower energy levels (e.g., Jacobi Integral  $<3.000$ ), the relationship reverses: the deviation of robust solutions from the invariant

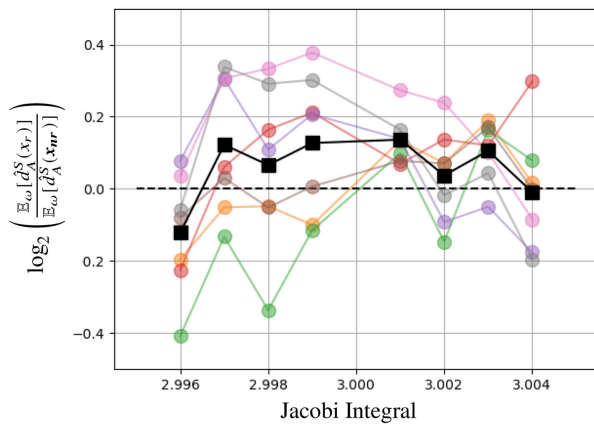
manifolds decreases as  $\Delta\tau$  increases. This suggests that robust solutions actively minimize deviation from the manifolds at earlier energy levels to counterbalance the larger deviations that occur at later stages of the transfer. This adaptive behavior appears to effectively reduce the average deviation across the entire trajectory, allowing robust solutions to maintain overall feasibility despite the increasing challenges posed by longer MTEs.

A similar trend is observed for  $\hat{d}_A^S$  (see Fig. 14). At earlier energy levels, as  $\Delta\tau$  increases, robust solutions exhibit a complex behavior: they move closer to the invariant manifolds and simultaneously progress farther along the manifold, distancing themselves from the associated periodic orbit. In contrast, at later energy levels, the behavior shifts. As  $\Delta\tau$  increases, robust solutions may drift further away from the invariant manifolds. However, they remain closer to the periodic orbits, indicating a strategic adaptation to the dynamical environment. By prioritizing proximity to periodic orbits at this stage, robust solutions mitigate the risks associated with chaotic dynamics near the end of the transfer.

As indicated in Table 3, the number of feasible robust solutions decreases with increasing  $\Delta\tau$ . Nonetheless, the solutions that remain feasible achieve this by strategically leveraging the geometry of the invariant manifolds. The value of  $\Delta\tau$  plays a pivotal role in shaping the feasibility and performance of robust solutions. Larger values of  $\Delta\tau$  necessitate a greater reliance on the geometric structure of invariant manifolds to maintain feasibility, which may come at the cost of higher fuel consumption. Across all feasible solutions, a larger  $\Delta\tau$  generally correlates with greater average distances from the invariant manifolds. However, within the subset of optimal solutions, robust trajectories continue to “shadow” the invariant manifolds as closely as, and in some cases even more closely than,



a) Feasible solutions



b) Optimal solutions

Fig. 14 Fold change in  $\hat{d}_A^S$  for robust solutions with varying  $\Delta\tau$  relative to nonrobust solutions.

nonrobust solutions. This demonstrates that longer MTEs do not necessarily preclude effective utilization of manifold dynamics.

Looking at the distance metrics associated with particular invariant manifolds can also reveal useful insights into the solutions. It can be intuitively surmised that the optimal LT solutions for this problem shall flow along  $W_U^{3:4}$  before eventually transitioning into  $W_S^{5:6}$ . To test this hypothesis, we evaluate the orthogonal distance to  $W_U^{3:4}$  and to  $W_S^{5:6}$ , i.e.,  $\bar{d}_T^S(W_U^{3:4})$  and  $\bar{d}_T^S(W_S^{5:6})$ , respectively, and the corresponding distance along the invariant manifold  $\bar{d}_A^S(W_U^{3:4})$  and  $\bar{d}_A^S(W_S^{5:6})$  for the optimal solutions in each category. As indicated by the increasing mean  $\bar{d}_T^S(W_U^{3:4})$  across energy levels, it is immediately obvious that the optimal solutions in all categories depart from  $W_U^{3:4}$  as they traverse the energy levels (Fig. 15a). Although we do not observe a converse trend in  $W_S^{5:6}$ , it is important to note that the

solutions remain consistently close to  $W_S^{5:6}$ , allowing them to leverage  $W_S^{5:6}$  whenever necessary (Fig. 15b).

On the other hand, the trend in  $\bar{d}_A^S$  indicates that, on average, the solutions remain relatively close to the 3:4 resonant orbit as they traverse the initial energy levels. However, as the energy levels increase, the solutions begin to drift away from the 3:4 resonant orbit, reflecting a gradual departure from its influence (Fig. 16a). Conversely, as the solutions progress through higher energy levels, there is a noticeable shift in alignment toward the 5:6 resonant orbit. This suggests that the trajectories increasingly rely on the DS associated with the 5:6 resonant orbit as they approach the later stages of the transfer, which, once again, aligns with our expectations (Fig. 16b).

In summary, as shown in Fig. 17, the overall feasible solution set for the robust case exhibits higher  $\hat{d}_T^S$  and  $\hat{d}_A^S$  values compared to the

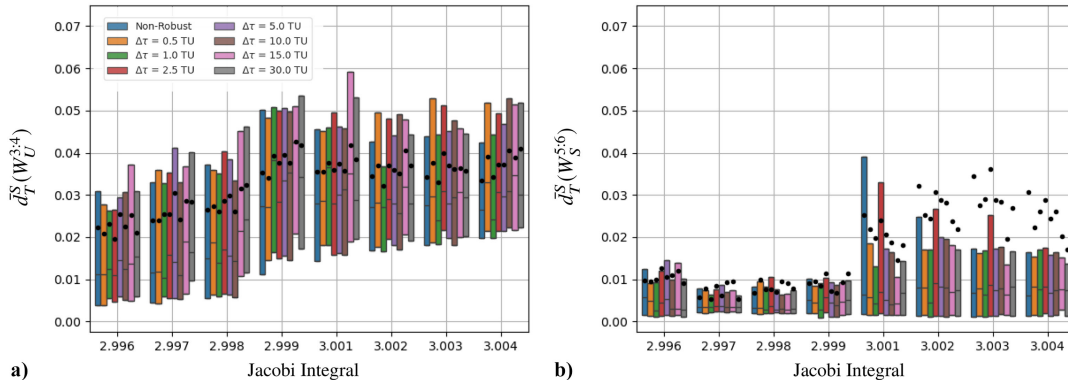


Fig. 15 The  $\bar{d}_T^S(W_U^{3:4})$  and  $\bar{d}_T^S(W_S^{5:6})$  for optimal nonrobust solutions and robust solutions with varying  $\Delta\tau$ .

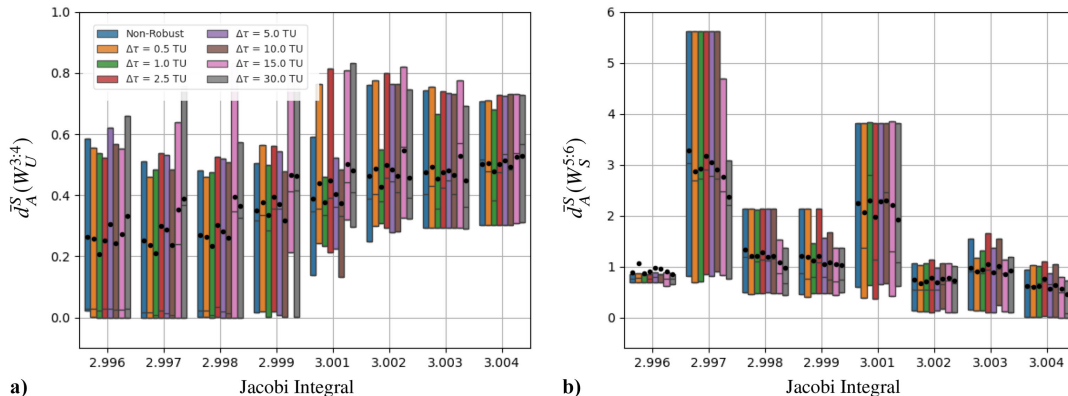


Fig. 16 The  $\bar{d}_A^S(W_U^{3:4})$  and  $\bar{d}_A^S(W_S^{5:6})$  for optimal nonrobust solutions and robust solutions with varying  $\Delta\tau$ .

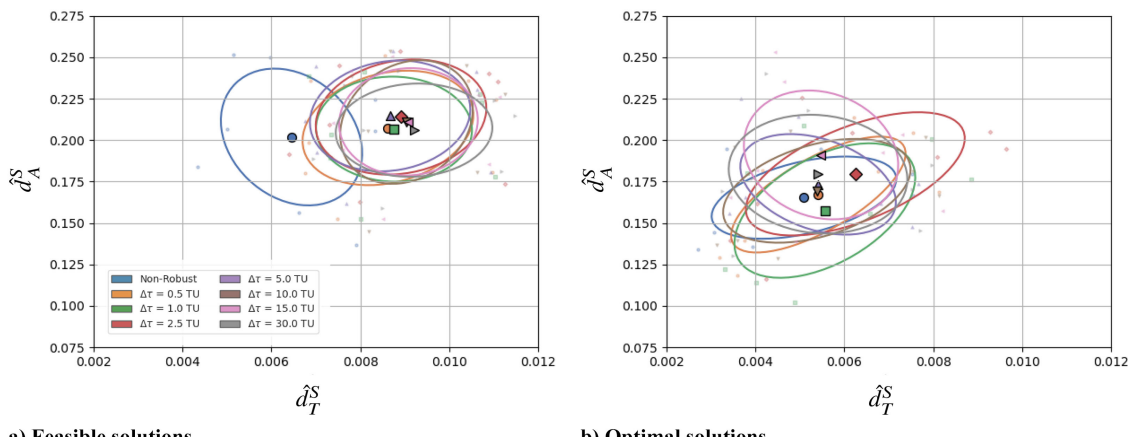


Fig. 17 The  $\hat{d}_T^S$  and  $\hat{d}_A^S$  with robust solutions categorized by  $\Delta\tau$ .

nonrobust case. However, if we only consider the optimal solutions, the mean  $\hat{d}_T^S$  for the robust solutions decreases, becoming more comparable to that of the nonrobust solutions. The shift in the mean between the feasible and optimal solutions suggests that, on average, the robust optimal solutions utilize the invariant manifolds as effectively as the nonrobust optimal solutions. The covariance ellipsoids, representing one standard deviation around the mean, reveal a larger spread in the robust solutions—particularly in the  $\hat{d}_A^S$  direction—suggesting greater variability in how the robust low-thrust solutions evolve along the invariant manifolds.

## 2. Dependence on $\tau_1$

In this section, we explore how the relationship of the robust solutions to the invariant manifolds changes as we vary  $\tau_1$ . We begin by grouping the solutions based on whether  $\tau_1$  occurs on the forward shooting arc (first half of the shooting horizon) or the backward shooting arc (second half of the shooting horizon) and performing similar analysis to those discussed in Sec. V.C.1. To distinguish between these two cases within the robust solution family, we will refer to the first case as “forward robust solutions” and the second as “backward robust solutions.”

For both the forward and the backward categories, the robust feasible solutions exhibit higher  $\hat{d}_T^S$  values compared to the nonrobust feasible solutions, with the backward robust solutions showing smaller distances than the forward robust solutions (Fig. 18a). However, when examining the optimal solutions, we observe that the forward robust solutions not only demonstrate a lower mean distance at the first energy level compared to the nonrobust solutions but also a lower mean distance than the backward robust solutions (Fig. 18b). Conversely, as the energy levels increase, the distance increases for the forward robust solutions and decreases for the backward robust solutions. If  $\tau_1$  occurs during the forward shooting arc, we expect robust solutions to adjust their control parameters to more effectively leverage the invariant manifolds at the initial energy levels; conversely, if  $\tau_1$  occurs during the backward shooting arc, the robust solutions are likely to make similar adjustments for the later energy levels. These expectations are consistent with the trends shown in Fig. 18. For both the forward and the backward robust solutions, it is important to note the greater reliance on the invariant manifolds for the robust solutions compared to the nonrobust solutions during the initial and final energy levels, respectively. We know that the absolute  $\hat{d}_T^S$  for both robust and nonrobust solutions decreases when considering the optimal solution subset—therefore, the fact that robust solutions shadow the invariant manifolds even more closely at certain energy levels highlights the greater reliance on the invariant manifolds for the robust optimal solutions dependent on where  $\tau_1$  occurs.

Note that  $\hat{d}_T^S(W_U^{3:4})$  increases across solution categories as we move through the energy levels (Fig. 19a). If we focus on the forward robust solutions, we observe that these solutions have a slightly smaller  $\hat{d}_T^S(W_U^{3:4})$  compared to the nonrobust solutions

during the first energy level. This is expected, as robust solutions that experience an MTE early in the trajectory are likely to leverage  $W_U^{3:4}$  more closely to compensate for the MTE. A similar pattern is observed for  $\hat{d}_T^S(W_S^{5:6})$  in robust backward solutions. These solutions are expected to align more closely with  $W_S^{5:6}$ , especially in the later energy levels, to mitigate the effects of an MTE in the latter half of the trajectory. Interestingly, these solutions maintain close alignment with  $W_S^{5:6}$  across all energy levels, which is logical because compensating for an MTE in the latter half requires the trajectory to remain close to  $W_S^{5:6}$  throughout, not just in the later stages (Fig. 19b).

If we examine  $\hat{d}_A^S(W_U^{3:4})$  and  $\hat{d}_A^S(W_S^{5:6})$  for the robust solution categories, we notice some interesting trends in the solutions. We do not notice any discernible pattern for the robust solutions with respect to  $\hat{d}_A^S(W_U^{3:4})$  (Fig. 20a), but we notice that the robust backward solutions demonstrate a smaller  $\hat{d}_A^S(W_S^{5:6})$  (Fig. 20b) compared to robust forward solutions, as well as the nonrobust solutions. This makes sense, as these backward arc solutions are expected to leverage the stable manifold  $W_S^{5:6}$  more closely, especially in the latter half of the trajectory. Interestingly, the robust forward solutions also maintain relatively small  $\hat{d}_A^S(W_S^{5:6})$  compared to the nonrobust solutions, especially toward the initial energy levels, suggesting that the robust forward solutions rely on  $W_S^{5:6}$ , similar to the robust backward solutions.

The dependence of robust solutions on  $\tau_1$  varies significantly depending on whether the MTE occurs along the forward or backward arc of the trajectory. When  $\tau_1$  is placed in the forward arc, robust solutions adjust their control profile early to compensate for the missed thrust earlier in the trajectory. This early adjustment typically results in closer alignment with unstable manifolds, such as  $W_U^{3:4}$ , at the earlier energy levels. Addressing the MTE at this stage ensures that the trajectory maintains sufficient stability to progress through the remainder of the transfer. Conversely, when  $\tau_1$  occurs in the backward arc, robust solutions modify their control profiles later in the transfer. These adjustments prioritize alignment with stable manifolds, such as  $W_S^{5:6}$ , at the later energy levels, facilitating seamless insertion into the target orbit. As shown in Fig. 21, interestingly, fuel consumption trends also differ based on the placement of  $\tau_1$ . Backward robust solutions typically exhibit lower fuel consumption compared to forward robust solutions, likely due to their increased reliance on stable manifold geometry during the final phases. From a cost-efficiency perspective, missed thrust events in the backward arc may be more favorable for this specific transfer.

As shown in Fig. 22, the averages  $\hat{d}_T^S$  and  $\hat{d}_A^S$  are lower for the optimal solution subset compared to the overall feasible solution set (Fig. 22). In the backward case, the robust optimal solutions behave more similarly to the nonrobust solutions. Because we expect the dynamics to be more chaotic during the backward shooting arc, it becomes necessary for the robust backward solutions to shadow the

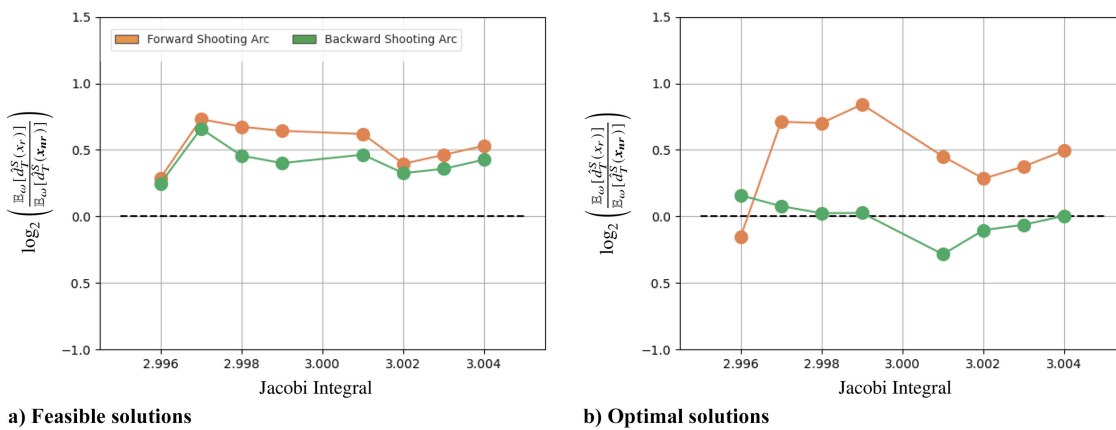


Fig. 18 Fold change in  $\hat{d}_T^S$  for robust solutions with varying  $\tau_1$  relative to nonrobust solutions.

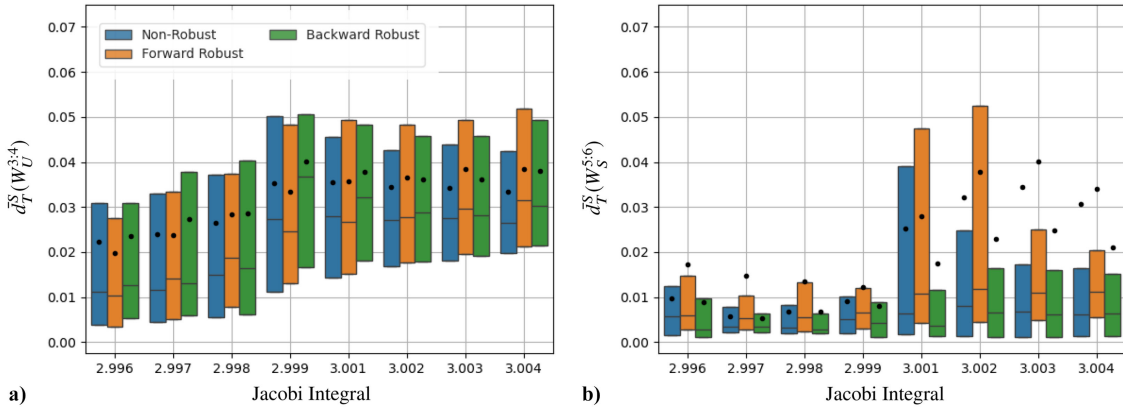


Fig. 19 The  $\bar{d}_T^S(W_U^{3:4})$  and  $\bar{d}_T^S(W_S^{5:6})$  for optimal nonrobust solutions and robust solutions with varying  $\tau_1$ .

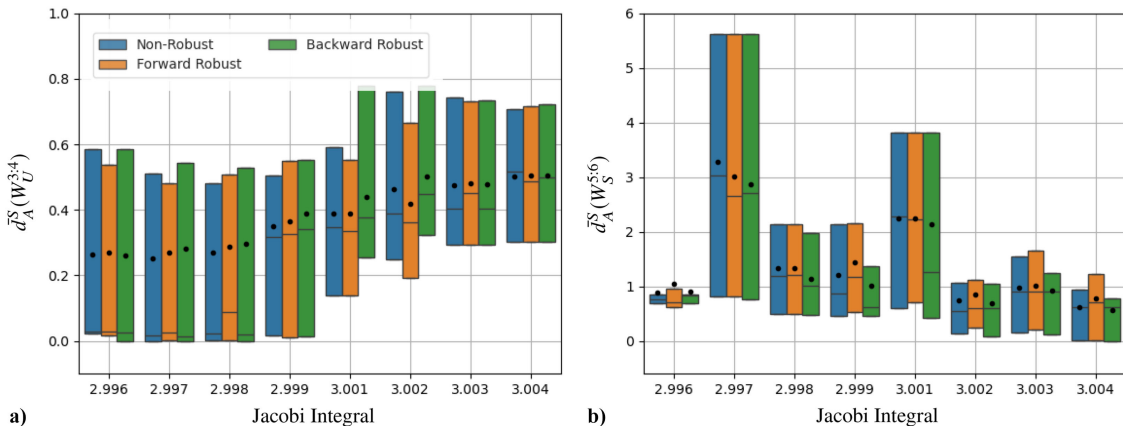


Fig. 20 The  $\bar{d}_A^S(W_U^{3:4})$  and  $\bar{d}_A^S(W_S^{5:6})$  for optimal nonrobust solutions and robust solutions with varying  $\tau_1$ .

invariant manifolds more closely. Although  $\hat{d}_T^S$  and  $\hat{d}_A^S$  decrease with the optimal solutions in relation to the feasible solutions, they remain higher for the robust forward case compared to the nonrobust solutions. Because the forward shooting segments are farther away from Europa, it is not as crucial for the robust forward solutions to leverage the invariant manifolds as strongly as the robust backward solutions.

The distinction between forward robust and backward robust solutions lies in the timing of the MTE along the trajectory. Forward robust solutions are designed with the assumption that the MTE occurs early in the transfer. These solutions allocate greater control margin during the initial phases and rely heavily on unstable mani-

folds to ensure stable progress after the MTE. Backward robust solutions, on the other hand, assume an MTE occurs later in the trajectory, typically near the terminal phases. These solutions preserve control margin and contingency fuel for the final approach, leveraging stable manifolds to achieve robust insertion into the target orbit. In practical mission design, forward robust strategies may be preferable when uncertainties are concentrated during the departure phase, while backward robust strategies are critical for ensuring accuracy and robustness during final orbital insertion or rendezvous, particularly when late-stage uncertainties are more pronounced.

The results demonstrate a strong dependence on the Jacobi energy level, which evolves over time as the spacecraft performs maneuvers. The Jacobi integral fundamentally determines which resonant orbits and associated manifolds are accessible to the trajectory, and these structures exhibit distinct geometries and stability characteristics at different energy levels. At lower energy levels, trajectories primarily rely on earlier resonances, such as those associated with  $W_U^{3:4}$ , to facilitate stable departure from the initial orbit. Here, unstable manifolds play a critical role in guiding the spacecraft through chaotic regions. As the energy levels increase, the trajectory transitions to leveraging stable manifolds tied to later resonances, such as  $W_S^{5:6}$ , to ensure stability and robustness during final approach and orbital insertion. This dependence on the Jacobi energy level reflects how the dynamical environment evolves across the transfer and highlights the adaptive strategies employed by robust solutions. By aligning with the most advantageous manifolds at each stage, robust solutions effectively balance stability and feasibility under varying constraints, including missed thrust events.

In addition to analyzing the relationship between each solution family and the invariant manifolds, we also compare the solution sets using two additional metrics that provide deeper insight into the solution behavior:

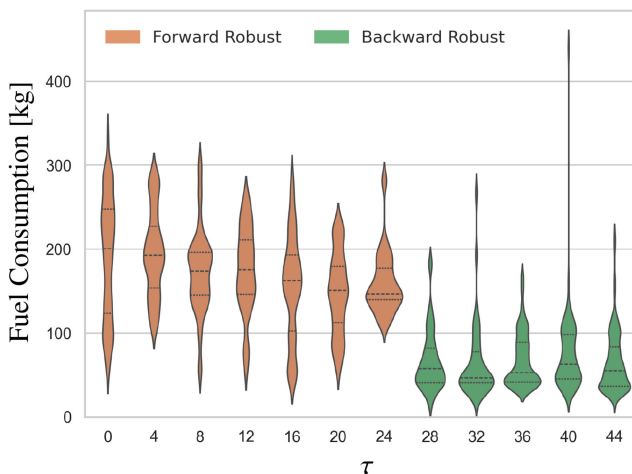


Fig. 21 Fuel consumption of robust solutions, categorized by  $\tau_1$ .

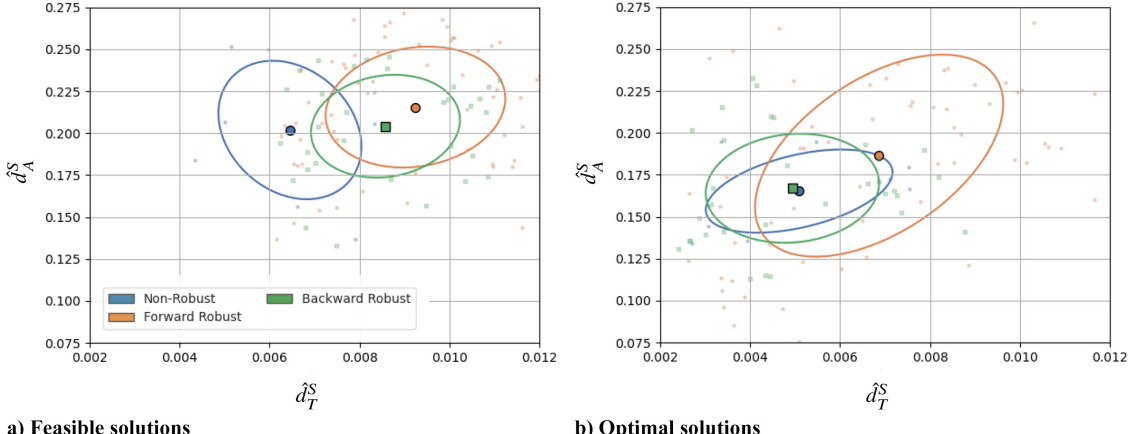


Fig. 22 The  $\hat{d}_T^S$  and  $\hat{d}_A^S$  with robust solutions categorized by  $\tau_1$ .

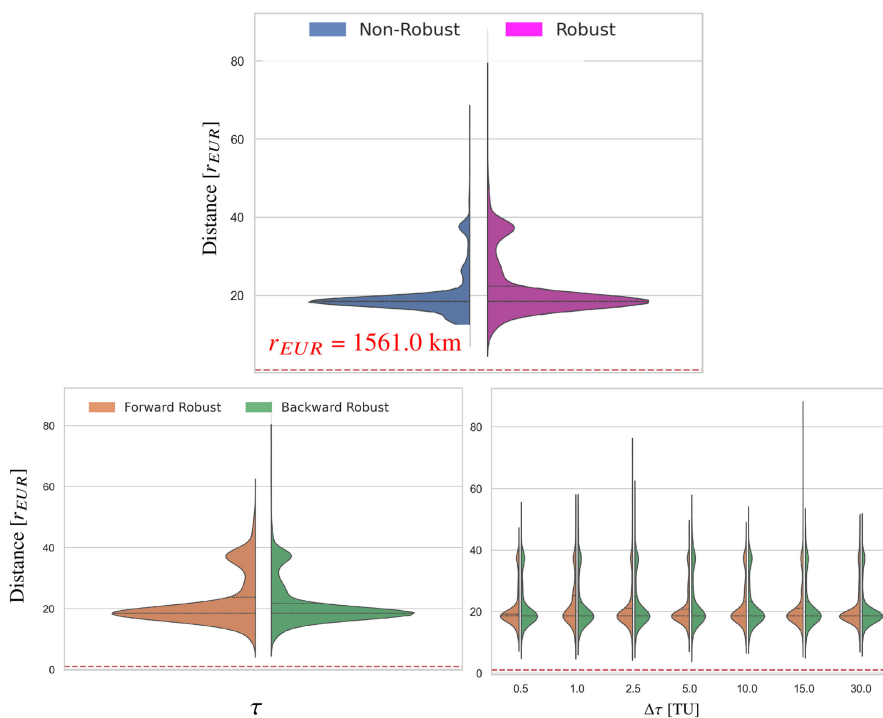


Fig. 23 Minimum distance to Europa.

**1) Distance to Europa:** In Fig. 23, we demonstrate the distribution of the minimum distance to Europa for both the robust and nonrobust solution sets. If we consider the entire robust optimal solution set, we observe the minimum distances tend to cluster around a broader range, whereas the nonrobust solutions show a narrower spread. The means for both sets look similar, but it is important to highlight that there exist some robust solutions that undergo very close approaches. To achieve optimality in the robust scenario, a balance needs to be struck between effectively leveraging the chaotic dynamics near the secondary while ensuring contingency in thruster operations by avoiding the chaotic regime near the secondary. We also observe a notable difference in the minimum distances between the forward and backward robust solutions, with the forward solutions exhibiting a tighter clustering around a narrower range. This contrast is particularly significant for the backward robust solutions, where MTEs may occur near the spacecraft's insertion into the terminal orbit. In these scenarios, it becomes necessary to either avoid the chaotic dynamics associated with close approaches to the secondary body or, conversely, to leverage these dynamics to facilitate a seamless insertion. The majority of backward robust solutions exploit the stable manifold geometry to

mitigate the effects of potential MTEs, effectively using the manifold's geometry to maintain feasibility, which is consistent with the stronger alignment we observe between the backward robust solutions and the invariant manifolds, compared to the forward robust solutions (see Fig. 22). However, there are some backward solutions that maintain greater distances from Europa, likely as a strategy to avoid the increased risk of chaos-induced infeasibility. The minimum distance to Europa is primarily determined by the alignment that best supports the manifold geometry for the given trajectory.

**2) Thrust arcs:** To further clarify these trends, we investigate the placement of the thrust arcs across solution families shown in Fig. 24. For nonrobust solutions, there are critical areas in the domain that "light up," suggesting that a majority of the solutions are placing the thrust arcs at critical transitions between manifolds, allowing the spacecraft to precisely transition between manifolds. In contrast, for the robust solutions, the solutions demonstrate a wider variance evident by the "smoother" heatmap (it is important to note the difference in magnitude between the nonrobust and the robust solutions). We observe that the forward robust solutions show activity near Europa, while the backward robust solutions have substantially lower activity in that region.

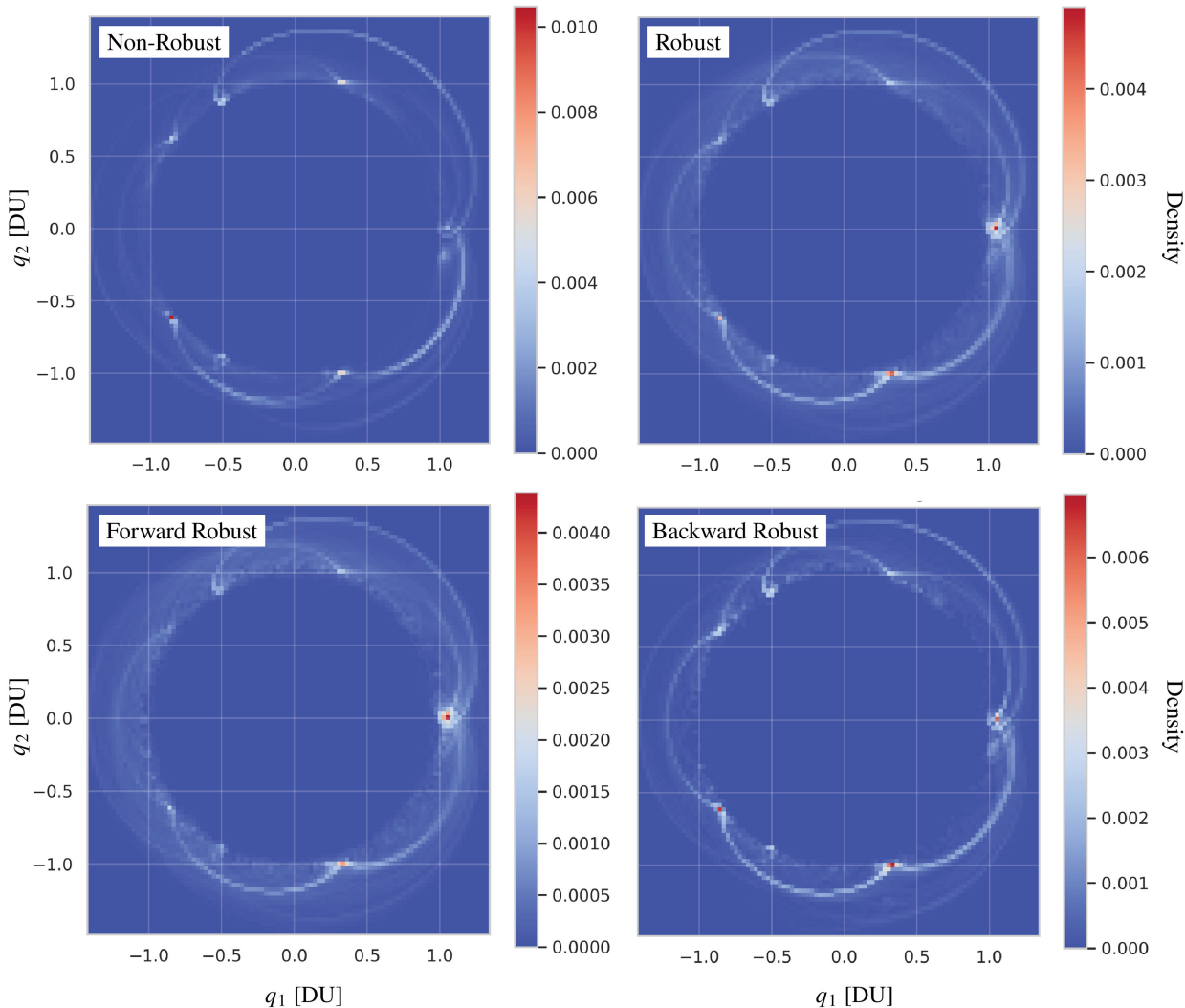


Fig. 24 Placement of thrust arcs.

These metrics provide additional insight into how the robust solutions compensate for the MTEs, as compared to their nonrobust counterparts. Overall, our findings confirm that the robust solutions do indeed rely on carefully chosen thrust-arc placements and systematically different flybys to mitigate the risks of MTEs. Consequently, the distance metrics, minimum altitudes, and thrust-arc placements collectively paint an informative picture of the tradeoffs inherent in designing robust versus nonrobust LT transfers within chaotic multibody dynamical systems.

#### D. Extensibility of Framework

The physical interpretation of these results highlights the differences in how nonrobust and robust solutions handle the possibility of MTEs. Nonrobust solutions assume uninterrupted thrust availability, which allows them to optimize for continuous LT maneuvers. However, this assumption leaves them highly vulnerable to deviations if an unexpected MTE occurs, as they lack contingency measures to recover. In contrast, robust solutions are explicitly designed to account for the possibility of a thrust outage, whether it occurs in the forward or backward arc. By incorporating this contingency, robust solutions adjust their trajectories to remain near the relevant invariant manifolds during critical periods, preserving both stability and feasibility despite the missed thrust event. From a physical standpoint, robust solutions sacrifice some nominal efficiency to leverage the stabilizing influence of manifold structures, enabling them to maintain robustness under challenging conditions. Our analysis demonstrates that invariant manifolds play a

critical role in LT trajectory design, which becomes more prominent when the solutions are made robust to missed thrust events. While our work focuses on a specific transfer, we highlight three ways in which these insights can be informative in other contexts:

**1) Analyzing relationships to invariant structures in multi-body dynamical systems:** Our framework can apply to more general celestial mechanics problems, as long as these problems possess similar DS. The core concept involves defining a distance metric to quantitatively study the relationship between (robust) LT solutions and invariant structures. While, in this paper, we study a planar circular restricted three-body problem, partially due to the ease in visualization this approximation permits, these techniques can be extended to not just other three-body problems but more generally to other multibody dynamical systems. In more complex problems, the LT solutions and the invariant structures may exhibit an increase in dimensionality, and therefore, the challenge in applying these methods will rely on the development of dynamical systems tools to efficiently generate these invariant structures. However, once we have these invariant structures, whether through data-driven approaches or other parameterization methods, the distance metrics can be readily extended to study the relationship between the LT solutions and the invariant manifolds, making the findings relevant to various mission design scenarios, including cislunar and interplanetary.

**2) Improving (robust) LT trajectory design through manifold geometry:** The strong correlation between the LT (robust) trajectory solutions and the invariant manifolds, as evident in this study, indicates the presence of valuable geometric constraints that can

significantly streamline the robust trajectory design process. For example, the astrodynamics software developed by Beeson et al. [30], which has been successfully applied to various cislunar problems—including the Power & Propulsion Element—demonstrates the value in embedding DS into the optimization process to streamline the automatic global search for solutions in complex environments. Furthermore, recognizing that (robust) solutions tend to align more closely with invariant manifolds can not only facilitate better initial guess generation for the control parameters but also improve the global search process since incorporating geometric knowledge into the robust trajectory design problem, either as a part of the objective function or as constraints, can help narrow the solution space.

**3) Understanding robustness through distance metrics:** We introduce distance metrics as proxies for evaluating robustness, correlating the extent to which solutions rely on invariant manifolds with their overall robustness. By investigating how varying the uncertainty parameters (e.g., where the MTE begins and how long they last) affect a trajectory's proximity to invariant structures, mission designers can proactively diagnose and thus mitigate potential performance degradations. This framework, therefore, can provide practitioners with a quantitative basis for providing statistical guarantees across diverse uncertainty realizations and actionable guidance for trajectory design.

While our current analysis focuses on planar, autonomous systems, the foundational concepts are general, extending to spatial and/or nonautonomous systems. In principle, a distance metric simply requires a representation—analytical or data-driven—of the underlying invariant sets in the dynamical system. As soon as a suitable approximation of these sets is available, the same distance metrics can be used to quantify how closely a given trajectory follows or diverges from the invariant structure. The main challenge in moving to three-dimensional scenarios is not the metric itself but rather the generation and representation of invariant objects in higher-dimensional spaces. Visualizing these manifolds also becomes difficult, as standard two-dimensional plots cannot fully capture the geometry, but advancements in visualization techniques have made progress in this area in recent years (e.g., [55–57]). Despite recent advancements, these methods still require numerically approximating the invariant structures. Numerical techniques for the automated approximation of center and invariant manifolds based on perturbation theory have been developed and applied to celestial mechanics in recent decades (e.g., [58–61]). A similar automated computer algebra approach to generating invariant manifolds has also been developed through the theory of Cabré et al. [62–64], named the *parameterization method for invariant manifolds*, and summarized in the book by Haro et al. [65]. Our methods can be further extended to address more complex dynamical models by generating approximations to dynamical structures as sets of data using the aforementioned techniques, wherein the benefits of a distance-based approach remain. Even if visual representations are less intuitive in higher dimensions, the metric itself continues to measure proximity between two sets—namely, an observed trajectory (or family of trajectories) and an invariant manifold. Thus, one can verify how close a given solution remains to an invariant structure without relying solely on graphical inspection. It is also possible to analyze nonautonomous systems through this framework by transforming them into autonomous systems through the extension of the phase space. This is achieved by converting a  $d$ -dimensional nonautonomous system into a  $(d+1)$ -dimensional autonomous system, where time is introduced as an additional state variable. In this extended phase space, traditional Poincaré sections can be defined by fixing time or event-based sections that trigger when specific state-space conditions are met. However, the distance metrics would now become time-dependent to account for invariant structure evolution over time. Beyond this modification, the techniques and distance metrics proposed in this study can be applied directly, enabling the analysis of these time-evolving manifolds while preserving the versatility of the framework.

## VI. Conclusions

The missed thrust design problem was formulated within a general robust optimal control framework that accounts for various forms of uncertainty. From this mathematical definition, a specific missed thrust design problem was defined, presenting it as a special case of the general robust optimal control problem. The study employed qualitative and quantitative tools to analyze the relationship between robust and nonrobust solutions and the underlying invariant manifolds. Using two distance metrics on a Poincaré section, the analysis revealed distinct differences in the behavior of feasible and optimal solutions for robust and nonrobust cases.

The results reveal that robust optimal solutions closely align with the relevant invariant manifolds, often matching or exceeding the alignment seen with nonrobust optimal solutions. This behavior underscores the critical role of invariant manifolds in facilitating robust trajectory design, particularly in maintaining optimality under missed thrust events. If the thruster outage occurs during the initial stages of the transfer, robust solutions exhibit closer alignment with the unstable invariant manifolds associated with the pertinent resonant orbits. Conversely, if the outage takes place during the later stages, robust solutions align more closely with the stable invariant manifolds of the pertinent resonant orbits. By leveraging these dynamical structures, robust solutions effectively mitigate the risks associated with thrust outages while maintaining trajectories that remain dynamically favorable. Having knowledge of the change in relation of a nonrobust to a robust trajectory with respect to the pertinent dynamical structures should enable more efficient solution methods to robust trajectory problems and, in particular, better enable the solution of these problems within a global optimization framework.

## Acknowledgments

The simulations presented in this article were performed on computational resources managed and supported by Princeton Research Computing, a consortium of groups including the Princeton Institute for Computational Science and Engineering (PICSciE) and the Office of Information Technology's High Performance Computing Center and Visualization Laboratory at Princeton University. The data that support this study are available from the authors upon reasonable request. The authors are grateful to the anonymous reviewers whose insightful comments and questions prompted substantial improvements in the presentation and interpretation of data that had been generated for the paper.

## References

- [1] Imken, T., Randolph, T., DiNicola, M., and Nicholas, A., "Modeling Spacecraft Safe Mode Events," *Proceedings of the 2018 IEEE Aerospace Conference*, IEEE Publ., Piscataway, NJ, 2018. <https://doi.org/10.1109/AERO.2018.8396383>
- [2] Rayman, M. D., Fraschetti, T. C., Raymond, C. A., and Russell, C. T., "Coupling of System Resource Margins through the Use of Electric Propulsion: Implications in Preparing for the Dawn Mission to Ceres and Vesta," *Acta Astronautica*, Vol. 60, No. 10, 2007, pp. 930–938. <https://doi.org/10.1016/j.actaastro.2006.11.012>
- [3] Oh, D., Landau, D., Randolph, T., Timmerman, P., Chase, J., Sims, J., and Kowalkowski, T., "Analysis of System Margins on Deep Space Missions Using Solar Electric Propulsion," *44th AIAA/ASME/SAE/ASEE Joint Propulsion Conference & Exhibit*, AIAA Paper 2008-5286, 2008. <https://doi.org/10.2514/6.2008-5286>
- [4] Madni, A. A., Hart, W., Imken, T., Oh, D. Y., and Snyder, S., "Missed Thrust Requirements for Psyche Mission," *AIAA Propulsion and Energy 2020 Forum*, AIAA Paper 2020-3608, 2020. <https://doi.org/10.2514/6.2020-3608>
- [5] Laipert, F. E., and Longuski, J. M., "Automated Missed-Thrust Propellant Margin Analysis for Low-Thrust Trajectories," *Journal of Spacecraft and Rockets*, Vol. 52, No. 4, 2015, pp. 1135–1143. <https://doi.org/10.2514/1.A33264>
- [6] Laipert, F. E., and Imken, T., "A Monte Carlo Approach to Measuring Trajectory Performance Subject to Missed Thrust," *28th AIAA/AAS*

- Space Flight Mechanics Meeting*, AIAA Paper 2018-0966, 2018.  
<https://doi.org/10.2514/6.2018-0966>
- [7] Olympio, J. T., "Designing Robust Low-Thrust Interplanetary Trajectories Subject to One Temporary Engine Failure," *20th AIAA/AAS Space Flight Mechanics Meeting*, AIAA Paper 2010-0171, 2010.
- [8] Rubinsztein, A., Sandel, C. G., Sood, R., and Laipert, F. E., "Designing Trajectories Resilient to Missed Thrust Events Using Expected Thrust Fraction," *Aerospace Science and Technology*, Vol. 115, May 2021, Paper 106780.  
<https://doi.org/10.1016/j.ast.2021.106780>
- [9] Ozaki, N., Campagnola, S., Funase, R., and Yam, C. H., "Stochastic Differential Dynamic Programming with Unscented Transform for Low-Thrust Trajectory Design," *Journal of Guidance, Control, and Dynamics*, Vol. 41, No. 2, 2018, pp. 377–387.  
<https://doi.org/10.2514/1.G002367>
- [10] Greco, C., Campagnola, S., and Vasile, M., "Robust Space Trajectory Design Using Belief Optimal Control," *Journal of Guidance, Control, and Dynamics*, Vol. 45, No. 6, 2022, pp. 1060–1077.  
<https://doi.org/10.2514/1.G005704>
- [11] Rubinsztein, A., Sood, R., and Laipert, F. E., "Neural Network Optimal Control in Astrodynamics: Application to the Missed Thrust Problem," *Acta Astronautica*, Vol. 176, June 2020, pp. 192–203.  
<https://doi.org/10.1016/j.actaastro.2020.05.027>
- [12] Izzo, D., and Öztürk, E., "Real-Time Guidance for Low-Thrust Transfers Using Deep Neural Networks," *Journal of Guidance, Control, and Dynamics*, Vol. 44, No. 2, 2021, pp. 315–327.  
<https://doi.org/10.2514/1.G005254>
- [13] Miller, D., and Linares, R., "Low-Thrust Optimal Control via Reinforcement Learning," *29th AIAA/AAS Space Flight Mechanics Meeting*, AIAA Paper 2019-0560, 2019, pp. 1–18.
- [14] Zavoli, A., and Federici, L., "Reinforcement Learning for Robust Trajectory Design of Interplanetary Missions," *Journal of Guidance, Control, and Dynamics*, Vol. 44, No. 8, 2021, pp. 1440–1453.  
<https://doi.org/10.2514/1.G005794>
- [15] Olympio, J. T., and Yam, C. H., "Deterministic Method for Space Trajectory Design with Mission Margin Constraints," *61st International Astronautical Congress*, International Astronautical Federation Paper IAC-10.C1.9.12, Paris, France, 2010, pp. 1–12.
- [16] McCarty, S. L., and Grebow, D. J., "Missed Thrust Analysis and Design For Low Thrust Cislunar Transfers," *AAS/AIAA Astrodynamics Specialist Conference*, AAS Paper 20-535, Springfield, VA, 2020.
- [17] Venigalla, C., Englander, J. A., and Scheeres, D. J., "Multi-Objective Low-Thrust Trajectory Optimization with Robustness to Missed Thrust Events," *Journal of Guidance, Control, and Dynamics*, Vol. 45, No. 7, 2020, pp. 1255–1268.  
<https://doi.org/10.2514/1.G006056>
- [18] Alizadeh, I., and Villac, B. F., "Sensitivity Reduction and Lifetime Extension of Power-Limited Low-Thrust Trajectories," *Journal of Guidance, Control, and Dynamics*, Vol. 36, No. 1, 2013, pp. 218–228.  
<https://doi.org/10.2514/1.56480>
- [19] Cox, A. D., Howell, K. C., and Folta, D. C., "Dynamical Structures in a Low-Thrust, Multi-Body Model with Applications to Trajectory Design," *Celestial Mechanics and Dynamical Astronomy*, Vol. 131, No. 3, 2019, Paper 12.  
<https://doi.org/10.1007/s10569-019-9891-7>
- [20] Cox, A. D., Howell, K. C., and Folta, D. C., "Trajectory Design Leveraging Low-Thrust, Multi-Body Equilibria and Their Manifolds," *The Journal of the Astronautical Sciences*, Vol. 67, No. 3, 2020, pp. 977–1001.  
<https://doi.org/10.1007/s40295-020-00211-6>
- [21] Cox, A. D., Howell, K. C., and Folta, D. C., "Transit and Capture in the Planar Three-Body Problem Leveraging Low-Thrust Invariant Manifolds," *Celestial Mechanics and Dynamical Astronomy*, Vol. 133, No. 5, 2021, Paper 22.  
<https://doi.org/10.1007/s10569-021-10022-y>
- [22] Anderson, R. L., and Lo, M. W., "Role of Invariant Manifolds in Low-Thrust Trajectory Design," *Journal of Guidance, Control, and Dynamics*, Vol. 32, No. 6, 2009, pp. 1921–1930.  
<https://doi.org/10.2514/1.37516>
- [23] Yong, J., and Zhou, X. Y., *Stochastic Controls: Hamiltonian Systems and HJB Equations*, Springer-Verlag, Berlin, 1999.  
<https://doi.org/10.1007/978-1-4612-1466-3>
- [24] Bertsekas, D. P., *Dynamic Programming and Optimal Control*, 3rd ed., Vol. I, Athena Scientific, Belmont, MA, 2005.
- [25] Bertsekas, D. P., *Dynamic Programming and Optimal Control*, 3rd ed., Vol. II, Athena Scientific, Belmont, MA, 2005.
- [26] Øksendal, B., *Stochastic Differential Equations: An Introduction with Applications*, 6th ed., Springer, Heidelberg, 2003.  
<https://doi.org/10.1007/978-3-642-14394-6>
- [27] Arnold, L., *Stochastic Differential Equations: Theory and Applications*, Wiley, New York, 1974.
- [28] Le Gall, J.-F., *Brownian Motion, Martingales, and Stochastic Calculus*, Springer, Cham, 2014.  
<https://doi.org/10.1007/978-3-319-31089-3>
- [29] Rudin, W., *Real and Complex Analysis*, 3rd ed., McGraw-Hill, New York, 1987, pp. 33–60, Chap. 2.
- [30] Beeson, R., Sinha, A., Jagannatha, B., Bunce, D., and Carroll, D., "Dynamically Leveraged Automated (N) Multibody Trajectory Optimization (DyLAN)," *AAS/AIAA Astrodynamics Specialist Conference*, AAS Paper 22-771, Springfield, VA, 2022.
- [31] Gill, P. E., Murray, W., and Saunders, M. A., "SNOPT: An SQP Algorithm for Large-Scale Constrained Optimization," *SIAM Review*, Vol. 47, No. 1, 2005, pp. 99–131.  
<https://doi.org/10.1137/S0036144504446096>
- [32] Wales, D. J., and Doye, J. P., "Global Optimization by Basin-Hopping and the Lowest Energy Structures of Lennard-Jones Clusters Containing up to 110 atoms," *Journal of Physical Chemistry A*, Vol. 101, No. 28, 1997, pp. 5111–5116.  
<https://doi.org/10.1021/jp970984n>
- [33] Leary, R. H., "Global Optimization on Funneling Landscapes," *Journal of Global Optimization*, Vol. 18, No. 4, 2000, pp. 367–383.  
<https://doi.org/10.1023/A:1026500301312>
- [34] Englander, J., Conway, B., and Williams, T., "Automated Interplanetary Mission Planning," *AAS/AIAA Astrodynamics Specialist Conference*, AAS Paper 12-4517, Springfield, VA, 2012.  
<https://doi.org/10.2514/5.9781624102714.0669.0706>
- [35] Englander, J. A., and Englander, A. C., "Tuning Monotonic Basin Hopping: Improving the Efficiency of Stochastic Search as Applied to Low-Thrust Trajectory Optimization," *24th International Symposium on Space Flight Dynamics*, Johns Hopkins Univ., Applied Physics Lab. Paper GSFC-E-DAA-TN14154, Laurel, MD, 2014.
- [36] Englander, J. A., and Conway, B. A., "Automated Solution of the Low-Thrust Interplanetary Trajectory Problem," *Journal of Guidance, Control, and Dynamics*, Vol. 40, No. 1, 2017, pp. 15–27.  
<https://doi.org/10.2514/1.G002124>
- [37] Sinha, A., and Beeson, R., "Comparative Study of Derivative Methods in Robust Low-Thrust Trajectory Design," *AAS/AIAA Astrodynamics Specialist Conference*, AAS Paper 25-191, Springfield, VA, 2025.
- [38] Ellison, D. H., "Robust Preliminary Design for Multiple Gravity Assist Spacecraft Trajectories," Ph.D. Thesis, Univ. of Illinois at Urbana-Champaign, Graduate College, Urbana, IL, 2007.
- [39] Szebehely, V., *Theory of Orbits: The Restricted Problem of Three Bodies*, Academic Press, New York, 1967.  
<https://doi.org/10.1016/B978-0-12-395732-0.X5001-6>
- [40] Koon, W. S., Lo, M. W., Marsden, J. E., and Ross, S. D., *Dynamical Systems, The Three-Body Problem and Space Mission Design*, World Scientific, Singapore, 2000.
- [41] Parker, J. S., and Anderson, R., *Low-Energy Lunar Trajectory Design*, Wiley, Hoboken, NJ, 2014.  
<https://doi.org/10.1002/9781118855065>
- [42] Poincaré, H., "Les méthodes Nouvelles De LA mécanique céleste, Tome 1, Gauthier-Villars, American Inst. Phys.," *New Methods of Celestial Mechanics, Parts 1*, 1892.
- [43] Hénon, M., "Exploration Numérique du Problème des Trois Corps, (I), Masses Égales, Orbites Périodiques," *Annales d'Astrophysique*, Vol. 28, No. 3, 1965, pp. 499–511.
- [44] Hénon, M., "Exploration Numérique du Problème des Trois Corps, (II), Masses Égales, Orbites Périodiques," *Annales d'Astrophysique*, Vol. 28, No. 6, 1966, pp. 992–1007.
- [45] Hénon, M., "Exploration Numérique du Problème des Trois Corps, (III), Masses Égales, Orbites Non Périodiques," *Bulletin Astronomique*, Vol. 1, No. 1, 1966, pp. 57–80.
- [46] Hénon, M., "Exploration Numérique du Problème des Trois Corps, (IV), Masses Égales, Orbites Non Périodiques," *Bulletin Astronomique*, Vol. 1, No. 2, 1966, pp. 49–66.
- [47] Hénon, M., "Exploration Numérique du Problème des Trois Corps, (V), Masses Égales, Orbites Non Périodiques," *Astronomy & Astrophysics*, Vol. 1, Feb. 1969, pp. 223–238.
- [48] Guckenheimer, J., and Holmes, P., *Nonlinear Oscillations, Dynamical Systems, and Bifurcations of Vector Fields*, 1st ed., Applied Mathematical Sciences, Springer, New York, 1983, pp. 1–65, Chap. 1.  
<https://doi.org/10.1007/978-1-4612-1140-2>
- [49] Wiggins, S., "Introduction to Applied Nonlinear Dynamical Systems and Chaos," *Texts in Applied Mathematics*, 2nd ed., Springer, New York, 2003, pp. 28–70, Chap. 3.  
<https://doi.org/10.1007/b97481>
- [50] Lo, M., "The InterPlanetary Superhighway and the Origins Program," *Proceedings of the 2002 IEEE Aerospace Conference*, IEEE Publ.,

- Piscataway, NJ, 2002, pp. 3543–3562.  
<https://doi.org/10.1109/AERO.2002.1035332>
- [51] Lam, T., “Ganymede to Europa in Mystic’s Circular Restricted Three Body Model,” Interoffice Memo, Jet Propulsion Lab., Europa Orbiter Project Archive, Pasadena, CA, Oct. 2004.
- [52] Whiffen, G., “Mystic: Implementation of the Static Dynamic Optimal Control Algorithm for High-Fidelity, Low-Thrust Trajectory Design,” *AIAA/AAS Astrodynamics Specialist Conference and Exhibit*, AIAA Paper 2006-6741, 2006.  
<https://doi.org/10.2514/6.2006-6741>
- [53] Restrepo, R. L., and Russell, R. P., “A Database of Planar Axisymmetric Periodic Orbits for the Solar System,” *Celestial Mechanics and Dynamical Astronomy*, Vol. 130, No. 7, 2018, Paper 49.  
<https://doi.org/10.1007/s10569-018-9844-6>
- [54] Gill, P. E., Murray, W., Saunders, M. A., and Wong, E., “SNOPT 7.7 User’s Manual,” Center for Computational Mathematics TR 18-1, Univ. of California, Oakland, CA, 2018.
- [55] Haapala, A. F., and Howell, K. C., “Representations of Higher-Dimensional Poincaré Maps with Applications to Spacecraft Trajectory Design,” *Acta Astronautica*, Vol. 96, March 2014, pp. 23–41.  
<https://doi.org/10.1016/j.actaastro.2013.11.019>
- [56] Geisel, C. D., “Spacecraft Orbit Design in the Circular Restricted Three-Body Problem Using Higher-Dimensional Poincaré Maps,” Ph.D. Thesis, School of Aeronautics and Astronautics, Purdue Univ., West Lafayette, IN, 2013.
- [57] Davis, D. C., Phillips, S. M., and McCarthy, B. P., “Trajectory Design for Saturnian Ocean Worlds Orbiters Using Multidimensional Poincaré Maps,” *Acta Astronautica*, Vol. 143, Feb. 2018, pp. 16–28.  
<https://doi.org/10.1016/j.actaastro.2017.11.004>
- [58] Jorba, A., “A Methodology for the Numerical Computation of Normal Forms, Centre Manifolds and First Integrals of Hamiltonian Systems,” *Experimental Mathematics*, Vol. 8, No. 2, 1999, pp. 155–195.  
<https://doi.org/10.1080/10586458.1999.10504397>
- [59] Jorba, A., and Masdemont, J., “Dynamics in the Center Manifold of the Collinear Points of the Restricted Three Body Problem,” *Physica D: Nonlinear Phenomena*, Vol. 132, No. 1, 1999, pp. 189–213.  
[https://doi.org/10.1016/S0167-2789\(99\)00042-1](https://doi.org/10.1016/S0167-2789(99)00042-1)
- [60] Gimeno, J., Jorba, A., Nicolás, B.n, and Olmedo, E., “Numerical Computation of High-Order Expansions of Invariant Manifolds of High-Dimensional Tori,” *SIAM Journal on Applied Dynamical Systems*, Vol. 21, No. 3, 2022, pp. 1832–1861.  
<https://doi.org/10.1137/21M1458363>
- [61] Gaeta, G. (ed.), *Perturbation Theory*, 1st ed., Springer, New York, 2022.  
<https://doi.org/10.1007/978-1-0716-2621-4>
- [62] Cabré, X., Fontich, E., and de la Llave, R., “The Parameterization Method for Invariant Manifolds I: Manifolds Associated to Non-Resonant Subspaces,” *Indiana University Mathematics Journal*, Vol. 52, No. 2, 2003, pp. 283–328.  
<https://doi.org/10.1512/iumj.2003.52.2245>
- [63] Cabré, X., Fontich, E., and de la Llave, R., “The Parameterization Method for Invariant Manifolds II: Regularity with Respect to Parameters,” *Indiana University Mathematics Journal*, Vol. 52, No. 2, 2003, pp. 329–360.  
<https://doi.org/10.1512/iumj.2003.52.2407>
- [64] Cabré, X., Fontich, E., and de la Llave, R., “The Parameterization Method for Invariant Manifolds III: Overview and Applications,” *Journal of Differential Equations*, Vol. 218, No. 2, 2005, pp. 444–515.  
<https://doi.org/10.1016/j.jde.2004.12.003>
- [65] Haro, A., Canadell, M., Figueras, J.-L., Luque, A., and Mondelo, J. M., *The Parameterization Method for Invariant Manifolds*, 1st ed., Springer, Cham, 2016.  
<https://doi.org/10.1007/978-3-319-29662-3>

M. Vasile  
*Associate Editor*